CATALYTIC METAL HYDROXIDE NANOSTRUCTURES: AEROBIC C-H ACTIVATION AND CATALYTIC LOW TEMPERATURE CARBON MONOXIDE OXIDATION BY $Ni_xMn_{(1-x)}(OH)_2$

A THESIS SUBMITTED TO

THE DEPARTMENT OF CHEMISTRY

AND THE GRADUATE SCHOOL OF ENGINEERING AND SCIENCE

OF BILKENT UNIVERSITY

IN PARTIAL FULFILLMENT OF THE REQUIREMENTS

FOR THE DEGREE OF

MASTER OF SCIENCE

IN

CHEMISTRY

By

Abel Tetteh Sika-Nartey

February 2021

I certify that I have read this thesis and that in my opinion it is fully adequate, in scope and in quality, as a thesis for the degree of Master of Science.

.....

Prof. Emrah Özensoy (Advisor)

I certify that I have read this thesis and that in my opinion it is fully adequate, in scope and in quality, as a thesis for the degree of Master of Science.

.....

Assist. Prof. Dr. Burak Ülgüt

I certify that I have read this thesis and that in my opinion it is fully adequate, in scope and in quality, as a thesis for the degree of Master of Science.

.....

Assist. Prof. Dr. Yunus Emre Türkmen

I certify that I have read this thesis and that in my opinion it is fully adequate, in scope and in quality, as a thesis for the degree of Master of Science.

.....

Assist. Prof. Dr. Ferdi Karadaş

I certify that I have read this thesis and that in my opinion it is fully adequate, in scope and in quality, as a thesis for the degree of Master of Science.

.....

Assoc. Prof. Dr. Görkem Günbaş

Approved for the Graduate School of Engineering and Science:

.....

Prof. Dr. Ezhan Karaşan

Director of the Graduate School

ABSTRACT

CATALYTIC METAL HYDROXIDE NANOSTRUCTURES: AEROBIC C-H ACTIVATION AND CATALYTIC LOW TEMPERATURE CARBON MONOXIDE OXIDATION BY $Ni_xMn_{(1-x)}(OH)_2$

Abel Tetteh Sika-Nartey
M.S. in Chemistry
Supervisor: Prof. Dr. Emrah Özensoy
February 2021

Metal hydroxides and mixed metal hydroxides have been frequently utilized in diverse applications such as battery technologies, electrocatalysis, electrosynthesis, photocatalysis, supercapacitors, electrochromic devices, and electrochemical sensors. Yet, precious metal-free hydroxides have not been utilized to their full potential in the field of catalytic aerobic C-H activation and catalytic low-temperature CO oxidation. In this work, we demonstrate that upon careful optimization of catalyst synthesis protocols, a novel catalytic architecture is achieved in the form of $Ni_{0.6}Mn_{0.4}(OH)_2$ revealing remarkable catalytic performance in the aerobic oxidation of alkylarenes, particularly in the aerobic oxidation of xanthene to xanthone. This optimized catalyst also shows superior catalytic activity in low-temperature CO (g) oxidation. We also present an efficient catalytic regeneration protocol, which can redeem the full initial activity of the carbon-poisoned spent catalyst in xanthene oxidation. Catalytic functionality of this novel nanomaterial architecture is also examined in detail in light of comprehensive characterization experiments including ATR-IR, XRD, BET-SSA, TGA, TEM, EDX and XPS measurements.

ÖZET

KATALİTİK METAL HİDROKSİT NANOYAPILARI: $Ni_xMn_{(1-x)}(OH)_2$ İLE OKSİJENLİ ORTAMLARDA C-H AKTİVASYONU VE DÜŞÜK SICAKLIKTA KARBON MONOKSİT YÜKSELTGENMESİ

Abel Tetteh Sika-Nartey
Kimya Yüksek Lisans Tezi
Danışman: Prof. Dr. Emrah Özensoy
Şubat 2021

Metal hidroksitler ve karışık metalli hidroksitler, batarya teknolojileri, elektrokataliz, elektrosentez, fotokataliz, süperkapasitörler, elektrokromik cihazlar ve elektrokimyasal algılayıcılar gibi bir çok uygulamada yaygın şekilde kullanılmaktadır. Ancak, değerli metal içermeyen hidroksitler, oksijenli ortamlarda katalitik C-H aktivasyonu ve düşük sıcaklıklarda katalitik CO oksidasyonu uygulamalarında henüz değerlendirilmemektedir. İşbu çalışmada, katalizör sentezleme protokollerinin dikkatli şekilde optimizasyonu sayesinde, yeni nesil $Ni_{0.6}Mn_{0.4}(OH)_2$ yapısında karışık metalli katalitik nanoyapılar sentezlenmiş ve bu malzemelerin, alkilarenlerin oksijenli ortamlarda katalitik olarak yükseltgenmesi ve düşük sıcaklıklarda katalitik karbon monoksit yükseltgenmesi tepkimelerinde üstün başarı sağladığı gösterilmiştir. Ayrıca, edilen bu yeni nesil katalizörlerin katalitik tepkimelerde kullanılmasının ardından, yüksek bir başarımla rejenerasyonunun sağlanmasına yönelik bir deneysel protokol geliştirilmiştir. Sentezlenen bu yeni nesil nano-malzemelerin işlevsel özelliklerinin kökenlerinin aydınlatılması adına, detaylı karakterizasyon çalışmaları yapılmıştır. Bu bağlamda, gerçekleştirilen ATR-IR, XRD, BET-SSA, TGA, TEM, EDX ve XPS deneyleri kimyasal yapı ve katalitik işlev arasındaki ilişkilerin açıklanmasını sağlamıştır.

Dedicated to the Glorious Memories of:

Christiana Korkor Saanor Laryea

A.S.I. Felicia Sika-Nartey

ACKNOWLEDGEMENTS

First, I would like to thank Jehovah God for the gift of life. I would also like to express my sincere gratitude and appreciation to special individuals who have supported me through the course of this journey.

I say a big thank you to Professor Dr. Emrah Özensoy. This work would not have been possible without his tutelage, guidance and support. It has been a pleasure to work in his research group. Thus, I say a big thank you to the whole Özensoy research group especially Kerem Emre Ercan.

In addition, I would like to thank Professor Dr. Yunus Türkmen and the Türkmen group for their collaboration on this work. Especially, Yeşim Şahin who aided in carrying out most of the activity experiments. I also would like to thank my M.Sc. thesis committee members Dr. Burak Ülgüt, Dr. Ferdi Karadaş, and Dr. Görkem Günbaş.

Last but not the least; I would like to thank the Grand and Blessed Family for their unending love, support and prayers.

TABLE OF CONTENTS

LIST OF FIGURES

LIST OF TABLES

CHAPTER 1

1. INTRODUCTION

Three major catalyst systems are usually utilized in literature in non-photocatalyic heterogeneous oxidation reactions.[1-3] These are metal on metal oxide (M/MO_x) systems (e.g. Pt/Al_2O_3), metal oxide on metal oxide or activated carbon-based supports (MO_x/MO_x or MO_x/C) systems (e.g. VO_x/TiO_2, PdO_x/Carbon nanotubes) and metal incorporated zeolite systems (e.g. Rh@MFI zeolite). Many of these catalysts are highly efficient in high temperature reactions, however they often suffer from low-temperature catalytic activity. Only few catalytic systems have been reported to have significant low-temperature catalytic activity such as, Ru/Al_2O_3[4], Au/TiO_2[5], Pd/Charcoal[6], $CaLaScRuO_{6+\delta}$[7] and RuO_2−FAU(faujasite zeolite)[8] . These catalysts have been reported to be efficient in low temperature aerobic oxidation of alcohols. Furthermore, it should be noted that most of these catalysts are comprised of platinum group metals (PGMs) or precious metals, which are highly expensive.

The crystal structures of metal hydroxide systems are vulnerable to high temperatures as they can readily be converted into oxide phases at elevated temperatures. However, they can be still exploited in low temperature catalytic processes. Along these lines, precious metal-free metal hydroxide systems can be synthetically fine-tuned to exhibit unique 2D structures, morphology, electronic and magnetic properties for low temperature reactions. Yan et. al. reported that $Ni(OH)_2$ when combined with TiO_2 performed 90 times better than pure TiO_2 in the photocatalytic hydrogen production from water. [9] Also, Ran et. al. reported that 23 mol% $Ni(OH)_2$ supported on CdS nanorods revealed a 145 times higher catalytic activity than pristine CdS nanorods in the visible-light-driven photocatalytic hydrogen gas production and a 1.3 times better performance than that of 1 wt.% Pt/CdS. [10] Gao et al. showed that when α-$Ni(OH)_2$ was used as an electrocatalyst in alkaline media, it yielded better catalytic activity and durability in harsh conditions than the a state-of-the-art catalyst PGM catalyst, i.e. RuO_2 in oxygen evolution reaction (OER). [11] Nickel-based mixed metal hydroxide systems have been reported to exhibit unique magnetic properties and the effect of this property in catalysis is yet to be understood. Dating from the first half of the twentieth century, metal hydroxides and mixed metal hydroxides have been utilized in diverse applications such as applied fields are battery technologies, electrocatalysis, electrosynthesis, photocatalysis,

supercapacitors, electrochromic devices, and electrochemical sensors.[12] However, these materials have not been explored in the context of C-H activation and catalytic low-temperature carbon monoxide (CO) oxidation. In the current work, we demonstrate that novel mixed metal hydroxide heterogeneous catalytic systems with optimized nanostructures can serve as extremely active, selective, and stable catalytic materials in low-temperature C-H activation in liquid phase, as well as CO oxidation in gas phase.

CHAPTER 2

2. BACKGROUND

2.1. Metal Hydroxide Structures

2.1.1. Fundamental Crystal Forms of Metal Hydroxides

$Ni(OH)_2$ is arguably the most extensively studied catalytic metal hydroxide, while its mixed metal hydroxide versions (i.e. Ni-based bimetallic metal hydroxides) have also been investigated[74, 83-94]. $Ni(OH)_2$ is known to exist in the so called β-phase, and its pseudo polymorphic variant, the α-phase. [13] Pseudo-polymorphism is a phenomenon where external molecules (e.g. solvent molecules) occupy particular sites of the crystal lattice structure of a solid to yield a particular stoichiometry. [14] β- $Ni(OH)_2$ exists naturally as a theophrastite mineral[15] and is isostructural with $Mg(OH)_2$. [16] $Ni(OH)_2$ exhibiting this β-motif has a trigonal symmetry (See **Figure. 1**).

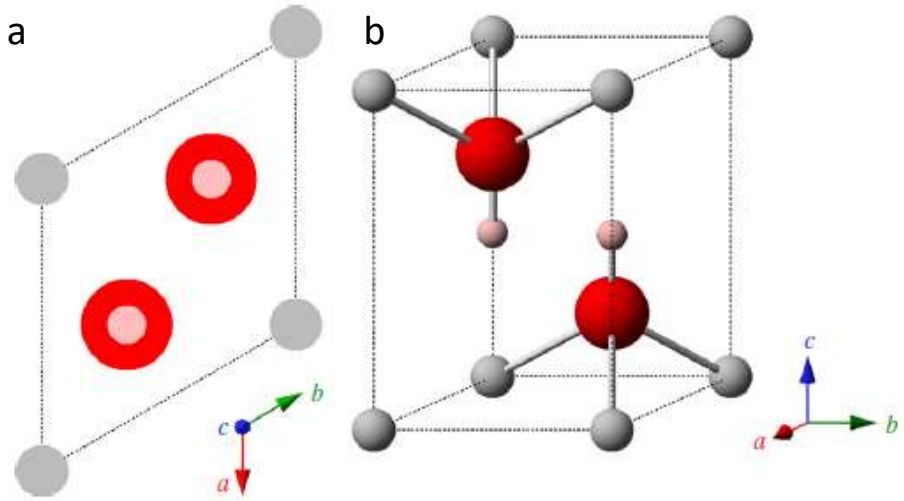

Figure 1. The crystal structure of β-$Ni(OH)_2$ represented by (a) unit cell projection and (b) ball-and-stick unit cell. Medium size (grey), large (red), and small (pink) spheres represent Ni^{2+}, O^{2-}, and H^+, respectively. [12]

The α- $Ni(OH)_2$ pseudo polymorph is intrinsically hydrated with H_2O molecules where the degree of hydration (x) varies within $0.41 \leq x \leq 0.7$, which can be represented as $[Ni(OH)_2.xH_2O]$. [17] Note that the correct representation of this hydrated pseudo polymorph is α- $Ni(OH)_2$ rather than α- $Ni(OH)_2.xH_2O$. α- $Ni(OH)_2$ is comprised of layers oriented parallel to the crystallographic ab-plane which are intercalated by water molecules (**Figure 2**). [13] In α -$Ni(OH)_2$, water serves as a

binding agent between the $Ni(OH)_2$ layers. This results in a poor orientation of adjacent layers and thus leading to the "turbostratic" structure of α-$Ni(OH)_2$, where the $Ni(OH)_2$ basal planes have slipped out of alignment. [18]

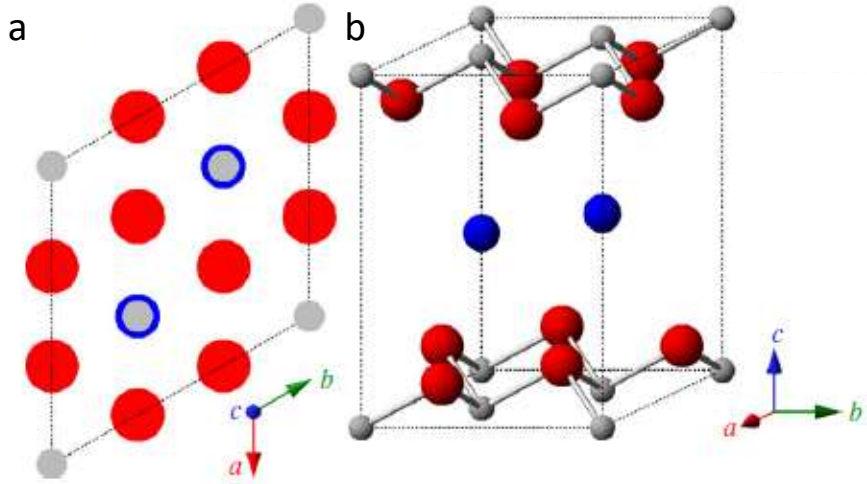

Figure 2. The idealized crystal structure of α-$Ni(OH)_2$ represented by (a) unit cell projection and (b) ball-and-stick unit cell for x =0.67 (actual value varies, $0.41 \leq x \leq 0.7$). Small (grey), large (red), and medium size (blue) spheres represent Ni^{2+}, OH^-, and H_2O, respectively. [12]

2.1.2. Structural Disorders in Metal Hydroxides

Although metal hydroxides exhibit two fundamental phases, structural disorders resulting from the incorporation of foreign ions, crystal defects such as stacking faults and variable hydration can lead to variations in these two fundamental phases. The type of structural disorder existing in the parent structure can lead to different denotations. For example, a β-$Ni(OH)_2$ with stacking fault disorder can be denoted as β_{bc}. [19] Structural disorders may play an important role in the chemical behavior of such systems. For instance, well-crystallized β-$Ni(OH)_2$ was reported to exhibit a lower electrochemical activity as compared to that of disordered β-$Ni(OH)_2$. [20]

2.1.2.1. Hydration

Taking $Ni(OH)_2$ as a case study, hydrated β-$Ni(OH)_2$, (i.e. $[Ni(H_2O)_x](OH)_2$, where $0.1 \leq x \leq 0.4$), have been reported to be highly active in electrochemical applications. These water molecules do not undergo hydrogen bonding with the lattice hydroxides and are weakly bound to the nickel cations. [21] Thermal gravimetric analysis (TGA) is used to characterize the amount of surface water and intercalated water in these samples. For example, TGA for hydrated β-$Ni(OH)_2$ shows that at 80-90 °C, surface water is removed but incorporated water may be fully eradicated only at 160 °C. [17, 22-24] Besides, it has been reported that there is a loss of 10-14% of charge capacity activity for thermally dehydrated β-$Ni(OH)_2$ in electrochemical applications. [25] Interlayer spacing in hydrated β-$Ni(OH)_2$ is about 0.1 Å greater than that of its dehydrated counterpart. [26] Attenuated Total Reflectance Infrared (ATR-IR) and Raman spectroscopic analyses are typically carried out to detect the presence of incorporated water in metal hydroxides. [22,26] As water is intrinsic to their structure, α-$Ni(OH)_2$ samples are always hydrated. TGA studies showed that compared to dehydrated β-$Ni(OH)_2$ samples, interlayer water in α-$Ni(OH)_2$ is removed at relatively higher temperatures of ca. 240-300 °C. [17,21,27] However, removal of interlayer water may occur concomitantly with the decomposition of the hydroxide to NiO. [21] On the other hand, in β-$Ni(OH)_2$, dehydroxylation occurs within 170-525 °C. [28]

2.1.2.2. Stacking Fault Disorder

Stacking faults in layered double hydroxides (LDHs) arise from the relatively weak bonds between adjacent layers. However, there exist relatively strong ionic bonds within the layers. [29] These faults can be detected by considering the oxygen anion stacking sequence. For instance in $Ni(OH)_2$, sequence alters from the ideal AC AC AC AC (**Figure 3**) to AC BA CB AC, etc. in the presence of stacking faults. [30-31] Also, in addition to the well-ordered thermodynamically favored structure, illustrated in **Figure 4a**, there exists other stacking motifs. **Figure 4b** illustrates stacking faults caused by a rotation about the crystallographic *c*-axis by 60°, while the structure shown in **Figure 4c** arises from the translation within the *ab*-plane. The third type of stacking fault occurs as a result of the combination of these former two stacking faults. [12] Stacking faults resulting from layer rotations cause selective line broadening in XRD patterns as the disorder is along the direction of

the crystallographic c-axis. [30] It must be noted that translational faults in ab-plane do not affect XRD peaks.

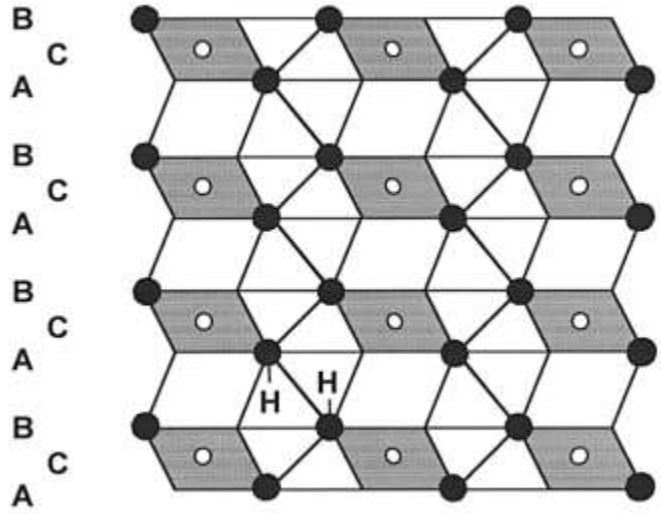

Figure 3. Section of the ideal structure of $Ni(OH)_2$ along the (110) plane. A and B sites are filled successively by oxygen atoms in the ideal structure and nickel ions are located at the C-site in the center. [31]

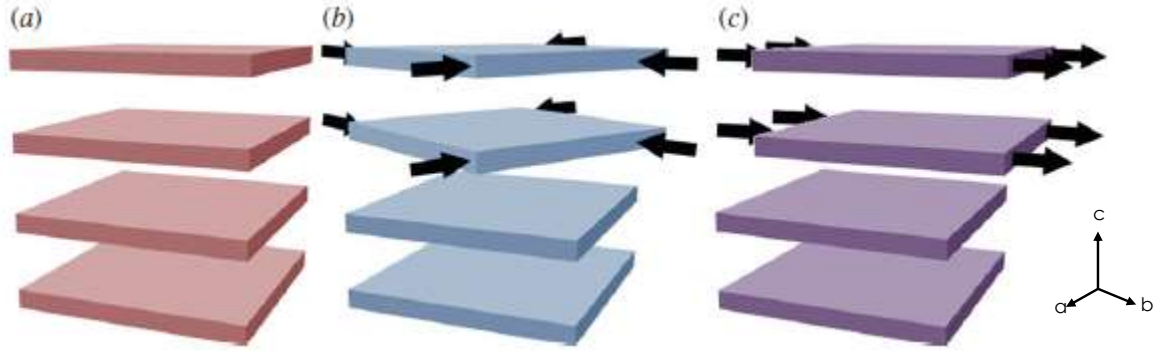

Figure 4. Stacking fault disorders between two adjacent layers. (a) No stacking faults are present and adjacent layers are aligned. (b) Rotation about the crystallographic *c*-axis. (c) Translation within the *ab*-plane. [12]

2.1.2.3. Ionic substitution and foreign ion incorporation

The substitution of a lattice atom (or polyatomic ion) with another species results in substitutional point defects. This is the most common defects found in nickel-based hydroxides. When a bivalent

metal cation (M) substitutes nickel cations, a $Ni_xM_{1-x}(OH)_2$ structure is obtained. **Figure 5** shows an α- $Ni(OH)_2$ with cationic substitutions of the lattice Ni with Mn. During the preparation method, some of the bivalent Mn oxidizes to Mn^{3+}. Oxidation of some of the Mn^{2+} species to Mn^{3+} results in the formation of two co-existing phases, namely, $Ni_xMn_{(1-x)}(OH)_2$ and a layered double hydroxides (LDH). In these two distinct phases, cation distributions are not the same. Incorporated anions either occupy lattice hydroxide sites or may sit within the interlayer region. The former tends to be less stable owing to the mechanical stresses due to ionic size mismatch. LDH phases may also incorporate NO_3^-, CO_3^{2-}, SO_4^{2-} or Cl^- anions to compensate the charge of +3 cations to maintain charge balance. This results in foreign ion incorporation to the structure, which leads to the observation of varying gallery heights, as illustrated in **Figure 5**. [32-33] However, it must be noted that β-$Ni(OH)_2$ samples are less likely to undergo foreign ion incorporation as the adjacent layers are closely packed.

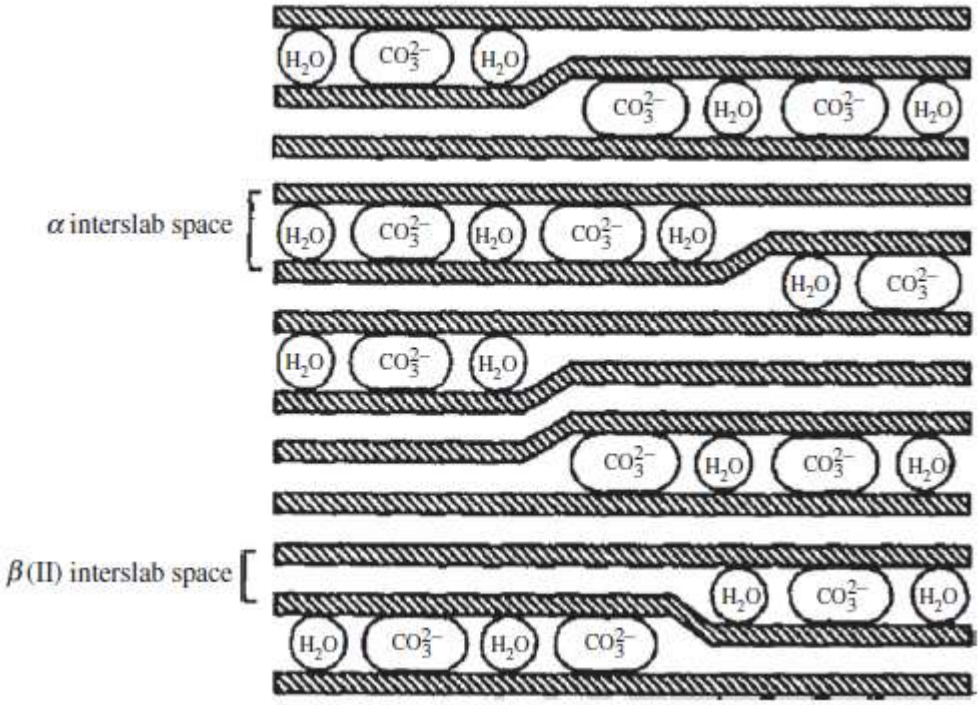

Figure 5. Schematic of α/β-interstratification. Here, both α and β-$Ni(OH)_2$ phases co-exist within a single crystal. Note that only α-$Ni(OH)_2$ layers contain intercalated carbonate anion impurities. [32]

2.1.2.4. α/β-Interstratification

In some metal hydroxides crystals, some of the layers are found to contain intercalated water (i.e., α-phase), whereas the rest are not (i.e., β-phase). These materials are defined as interstratified phases containing both α-type as well as β-type structural motifs within the same crystal rather than a simple mixture of the α and β crystals located in isolated domains.[32,34-36] This implies that these two different domains co-exist within a single crystal and such structures are denoted as α/β_{IS} (**Figure 5**). When there is a relatively high amount of this type of structural disorder, measured XRD patterns of the samples appear shifted and broadened. This is due to the fact that the long-range structural order needed for diffraction measurements are drastically reduced in interstratified materials. In the case where there is only one type of motif in a layer, the disorder is only oriented along the crystallographic *c*-axis. Hence, measured XRD peaks will be selectively broadened or in some cases, they may be lacking some of the peaks entirely. [36-37]

2.2. Metal Hydroxides and their Applications

One of the early applications of transition metal hydroxides were in battery technologies. In the first half of the 20th century, $Ni(OH)_2$ was used as an electrode material in battery applications. Hauel reported that $Ni(OH)_2$ combined with pure crystalline graphite served as an active anode material while the corresponding cathode active material was CdO or $Cd(OH)_2$. These materials performed exceptionally well. As a result, Cadmium-Nickel batteries were used in numerous commercial applications such as signal and mine lamps, train lighting, radio sets, flash lights and various types of military, emergency, medical, communication, electronic devices during the first half of the twentieth century. [38] Thus, metal hydroxides have gained much attention in practical applications like photocatalysis, electrocatalysis and electrosynthesis, supercapacitors, electrochromic devices, electrochemical sensors and catalytic dehydrogenation of boron-based materials.

Concerning their applications in supercapacitors, $Ni_{0.32}Co_{0.68}(OH)_2$ with an energy efficiency of 90% at 10 $A.g^{-1}$ has been reported to possess advanced capacitive performance when used as a positive electrode in asymmetric supercapacitors.[39] Also, $Al_{0.034}Ni_{0.966}$ LDH electrode was

proposed to be a promising material for pseudo-supercapacitors because of its relatively high charging and discharging rates. [40]

In electrochromic device applications, Mortimer et. al. demonstrated that $Ni(OH)_2$ films showed excellent transmittance modulation, attaining a maximum Δ%T of 83.2 at 432 nm. [41] Hierarchical macro-mesoporous $Ni(OH)_2$ when used as a glucose sensor showed good selectivity, excellent stability and reproducibility. This material was able to provide amperometric sensing of glucose with a wide linear range (0.01–8.3 mM), a high sensitivity of 243 μA mM cm^{-2} and a low detection limit of 1 μM. [42]

Ultrafine NiFe nanoparticles (NPs) decorated by $La(OH)_3$ were reported to exhibit excellent performance in the dehydrogenation of hydrazine borane ($N_2H_4BH_3$) and hydrous hydrazine ($N_2H_4.H_2O$) under alkaline conditions at 343 K. This catalyst had 35-fold higher turn-over-frequency (TOF) when compared to NiFe nanoparticles (NPs). [43]

2.3. Heterogeneous Aerobic oxidation of Alkylarenes and Alcohols to ketones.

Catalytic functionalization of inactivated C-H bonds by precious metal-free catalysts continues to be a challenge in the field of catalysis as it presents a huge opportunity to revolutionize the chemical industry. [44] For example, xanthone was reported to have diverse pharmacological properties. [96] Studies have shown that xanthone exhibit antithrombotic [97], antioxidant [98, 99], cardiotonic, vasorelaxant [100], antiulcer, choleretic, anti-inflammatory [101, 102], antiallergic, diuretic and monoamine oxidase (MAO) inhibitory activity [103]. In addition, xanthone derivatives come with additional pharmacological properties, as they are known for their potent antimicrobial, antiviral, cytotoxic, and antifungal activities. Additionally, they can be used as nutritional supplements that improve conditions in chronic inflammatory diseases and because of their antioxidant property; they are known to prevent premature aging. Thus, this class of compounds can be utilized as promising chemical scaffold for the development of new pharmacophores. [104] Numerous studies exist in the literature on the aerobic oxidation of alcohols [45] but this cannot be said for the alkylarenes. [46] Perovskites, precious PGM supported catalysts and metal oxides were utilized in the aerobic oxidation of alkylarenes (**Table 1**), while there exists a single study exploiting PGM-free metal hydroxides. [95]

Table 1. Literature data on heterogeneous catalytic aerobic oxidation of xanthene to xanthone.

Catalyst/ Additive	Xanthene[mmol]/ Catalyst[mg]/ Additive[mmol]	Oxidant / [atm]	Solvent/ Volume[mL]	Temp [°C]	Time [h]	Conversion [%]	Yield [%]	Ref.
Ni–MnO_x	0.2 / 20 / ---	O_2 / 1	n-octane/ 2	80	2	---	> 99	[47]
$BaFeO_{3-\delta}$	1.0 / 200 / ---	O_2 / 1	$PhCF_3$ / 1	90	96	---	95	[48]
$SrMnO_3$ –A. A	0.5 / 100 / ---	O_2 / 1	n-octane/ 2	80	12	---	82	[49]
$SrMnO_3$	1.0 / 200 / ---	O_2 / 1	n-octane/ 4	80	24	---	42	[50]
$LaMnO_3$	0.5 / 100 / --- & 0.5 / 50 / ---	O_2 / 1	Heptane / 2	80	24	>99 & 91	97 -	[51]
Co–NHAp / KOH	1.0 / 180 /0.5	Air / 1	p-xylene / 10	100	8	---	90	[52]
5 wt% Ir-TiO_2	1.5 / 75 / ---	O_2 / 1	Mesitylene / 1.5	150	12	>99	98	[53]
Shirasagi KL (Activated Carbon)	3.15 / 524 / ---	O_2 / 1	m-xylene / 5	120	50	---	94	[54]
$Ag_6[PV_3Mo_9O_{40}]$ nanorods	2.0 / 50 / ---	O_2 / 1	PhCN / 1	100	10	96.7	---	[55]
$CrCoFeO_4$@G–GO	1.0 / 120 / ---	Air / 1	o-xylene / 10	Reflux	4	90	---	[56]
2 wt. % Au–pDA–rGO / NHPI	1.0 / 20 / 0.1	O_2 / 10	CH_3CN / 5	60	10	90.5	---	[57]
CoPc@Cellulose / KOH, NHPI	1.0 / 50 / 0.25, 0.06	O_2 / 1	o-xylene / 5	Reflux	9	---	91	[58]
$Fe(NO_3)_3.9H_2O$ / KPF_6	1.0 / 40.4 / 0.2	O_2 / 1	CH_3CN / 3	80	2	---	95	[59]
$Ru(OH)_x/Al_2O_3$	1.0 / 50 / ---	O_2 / 1	$PhCF_3$ / 6	100	2	99	92	[60]

Cobalt-Chitosan / NHPI	1.0 / 23 / 1000	Air [15 mL min^{-1}]	1,2-dichlorobenzene / 10	80	4	---	95	[61]
MnO_2@wool	1.0 / 110 / ---	Air / 1	o-xylene / 5	Reflux	10	---	89	[62]
MnO_2/cellulose	1.0 / 100 / ---	Air / 1	o-Xylene / 15	120	13	---	94	[63]
N doped AC **Pd/AC** **Ru/AC**	1.0 / 100 / ---	Air / Autoclave	Toluene / 8	100	4	---	38 25 98	[64]
PC–MnO2 nanohybrid	1.0 / 40 / ---	Air / 1	p-xylene / 5	100	5	---	95	[65]
Mo-MnO_2	0.5 / 50 / ---	O_2 / 5	o-dichlorobenzene/ 1	150	3	---	88	[66]
Ni_2Mn-LDH	1.0/ 200/ ---	O_2 / 1	Dodecane / 2	120	1.5	98	---	[95]

2.4. Catalytic Carbon Monoxide Oxidation at Low Temperatures

Automobile emissions is a major contributor to global warming. With the aim of minimizing these emissions, low-temperature catalytic carbon monoxide (CO) oxidation studies have gained attention. [67] Scientific studies reveal that during vehicle cold-start regime, exhaust emissions – particularly CO and hydrocarbon (HC) emissions - accumulate to 50-80% emitted exhausts during the vehicle's entire drive cycle. [68] U.S. DRIVE has proposed a new challenge called the "150C challenge" encouraging the development of catalysts that can reach T_{90} (i.e., the temperature at which 90% exhaust (CO, NO) conversion is achieved) at temperatures < 150 °C. [69] Despite their high costs, PGM-based commercial benchmark catalysts perform poorly in CO and HC oxidation below 100 ºC. [70-71] On the other hand, some transition metal oxides, such as Co_3O_4 nanorods were reported to exhibit high activity towards CO oxidation close to ambient temperatures. [72-73] Low temperature CO oxidation is also a very important reaction in Proton Exchange Membrane (PEM) fuel cell applications, where the CO (which can poison the PGM catalysts in the fuel cell electrode) in the hydrogen feedstock needs to be oxidized at room temperature through the so called Preferential Oxidation (PROX) reaction. [105-106] Furthermore, CO oxidation is also used as the most

commonly utilized test reaction to screen the relative performance of novel oxidation catalysts with respect to conventional PGM-based benchmark catalysts (e.g., 1wt.% Pt/Al_2O_3). Thus, in the current work, we aimed to fine-tune the electronic, structural, magnetic and morphological properties of these precious metal-free transition-metal hydroxides for catalytic low temperature CO oxidation reactions.

CHAPTER 3

3. EXPERIMENTAL

3.1. Sample Preparation / Catalyst Optimization

In order to synthesize an optimized catalyst, four major synthetic parameters were investigated as discussed below.

3.1.2. Metal Precursor Type

During the synthesis of $Ni_xMn_{(1-x)(}OH)_2$ catalysts, some of the Mn^{2+} species are oxidized to Mn^{3+}. Mn^{3+} causes transformation of the single phase $Ni_xMn_{(1-x)(}OH)_2$ system into a two-phase system containing $Ni_xMn_{(1-x)(}OH)_2$ and LDH. In these two different phases, cation distributions are not the same. Incorporated anions either occupy lattice hydroxide sites or may be accomodated within the interlayer region. The former situation tends to be less stable owing to the mechanical stresses from ion size mismatch. LDH phases may incorporate NO_3^-, CO_3^{2-}, SO_4^{2-}, Cl^- anions to compensate the charge of +3 cations. Since the metal hydroxide synthesis protocols do not involve a high temperature treatment step, nitrate, carbonate and sulfate ions result in the release of toxic gases upon high temperature exposure of the synthesized material. [74] In order to minimize such toxicity risks, we preferred to use chloride precursors in the metal hydroxide synthesis. Accordingly, $NiCl_2.6H_2O$ (≥98% purity, Sigma-Aldrich) and $MnCl_2.2H_2O$ (≥99% purity Merck) were used as precursors in the catalyst synthesis.

3.1.2. Synthesis Method Optimization

Two different synthesis methods were utilized in the optimization of catalysts for the aerobic oxidation reactions. These were the solvothermal synthesis method (**Figure 6**) and the chemical precipitation method (**Figure 7**). In both methods, $NiCl_2.6H_2O$ (≥98% purity Sigma-Aldrich), $MnCl_2.2H_2O$ (≥99% purity Merck) and NaOH (≥98% purity Sigma-Aldrich) were used as precursors for the synthesis of $Ni_xMn_{(1-x)}(OH)_2$. Stoichiometric concentration of NaOH(aq) required for the synthesis of currently investigated metal hydroxides was 2.06M. Hereafter, this concentration will be denoted as "S". $Ni_{0.5}Mn_{0.5}(OH)_2$ catalyst, which was synthesized in 3S NaOH was used to compare catalytic performances corresponding to these two different synthesis methods (i.e., solvothermal vs. chemical precipitation).

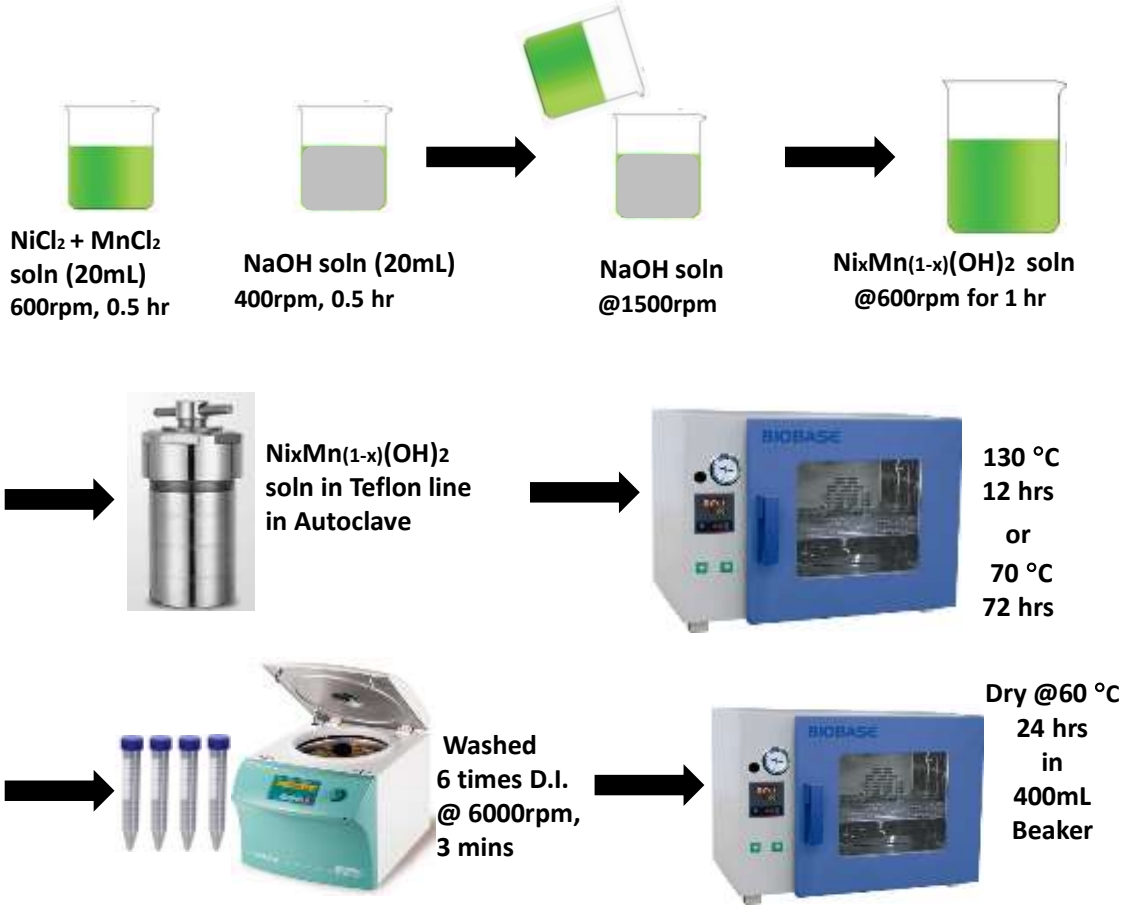

Figure 6. Illustration of $Ni_xMn_{(1-x)(}OH)_2$ synthesis via solvothermal method.

For the solvothermal method (**Figure 6**), proper amounts of $NiCl_2.6H_2O$ and $MnCl_2.2H_2O$ were dissolved in 20 ml deionized water. In addition, a proper amount of NaOH was dissolved separately in 20 ml deionized water. The former solution was stirred at 600 rpm and the latter at 400 rpm for a period of 0.5 h. Prior to mixing, stirring speed was increased to 1500 rpm and two solutions were mixed at his rate for 1 min. This mixture was further stirred at 600 rpm for 1 h after which it was immediately transferred into a Teflon line. Then, the Teflon line was inserted into an autoclave and heated in a drying oven at 130 ºC for 12 h or 70 ºC for 72 h. This mixture was washed 6 times with deionized water by centrifuging at a rate of 6000 rpm for 3 min in four different centrifuge tubes. This was followed by drying the obtained colloid in a 400 ml beaker at 60 ºC for 24 h. A similar procedure was used for the chemical precipitation method (**Figure 7**) but with the omission of the autoclave heating step.

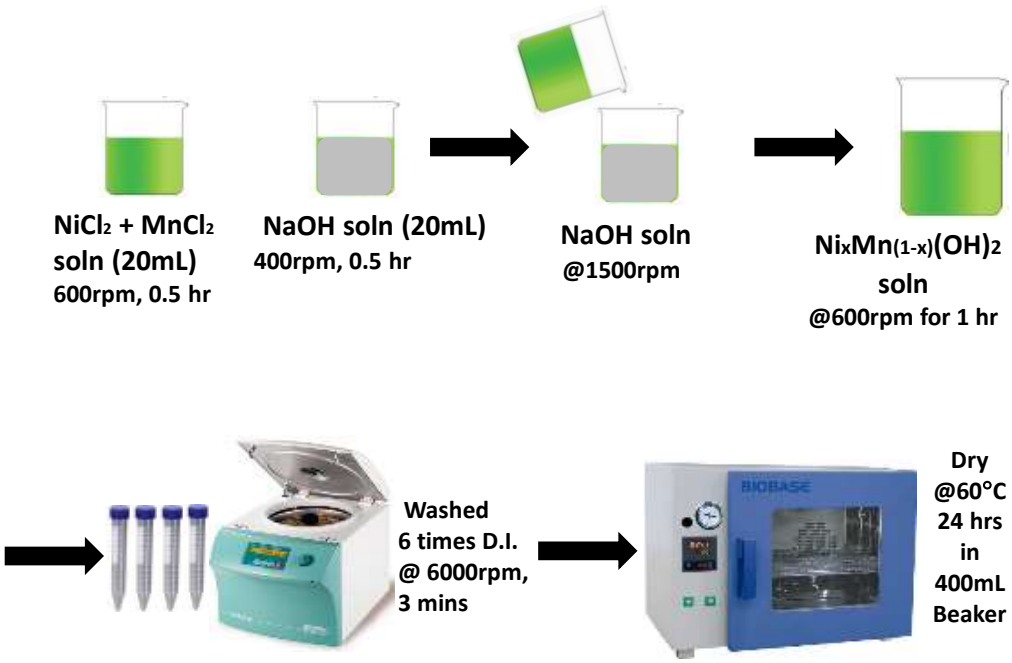

Figure 7. Illustration of $Ni_xMn_{(1-x)(}OH)_2$ synthesis by Chemical Precipitation method.

3.1.3. Metal Cation Stoichiometric Ratio Optimization

To find the optimized nickel-manganese hydroxide catalyst synthesized by the chemical precipitation method, which outperformed solvothermal method in terms of activity for the studied reaction (i.e., aerobic oxidation of xanthene to xanthone), nickel and manganese ratios were varied

whilst keeping the NaOH concentration constant at 6S. **Table 2** accounts for the amounts of nickel and manganese precursors used.

Table 2. The amount of chemicals used in the chemical precipitation synthesis method.

Sample	Mass of $NiCl_2.6H_2O$, g	Mass of $MnCl_2.6H_2O$, g	Mass of NaOH, g
$Mn(OH)_2$	-	3.3333	9.8845
$Ni_{0.5}Mn_{0.5}(OH)_2$	2.4473	1.6667	9.8845
$Ni_{0.6}Mn_{0.4}(OH)_2$	2.9368	1.3333	9.8845
$Ni_{0.7}Mn_{0.3}(OH)_2$	3.4263	0.9999	9.8845
$Ni_{0.8}Mn_{0.2}(OH)_2$	3.9157	0.6667	9.8845
$Ni_{0.85}Mn_{0.15}(OH)_2$	4.1605	0.4999	9.8845
$Ni_{0.9}Mn_{0.1}(OH)_2$	4.4052	0.3333	9.8845
$Ni_{0.95}Mn_{0.15}(OH)_2$	4.6499	0.1667	9.8845
$Ni(OH)_2$	4.8947	-	9.8845

3.1.4. NaOH Concentration Optimization

Metal cation stoichiometric ratio optimization experiments revealed that $Ni_{0.6}Mn_{0.4}(OH)_2$ exhibited the best performance in the aerobic oxidation of xanthene to xanthone. Using this optimal elemental ratio, the concentration of NaOH was varied to find the optimized catalyst. That is, the synthesis was carried out using 1S, 3S, 6S, 9S, 12S and 15S NaOH concentrations. Note that 15S corresponds to the saturation concentration of NaOH in water.

3.2. Instrumentation

3.2.1. Attenuated Total Reflectance Infrared (ATR-IR)

Bruker Alpha Platinum FTIR spectrometer equipped with a diamond ATR crystal module, and a deuterated triglycine sulfate (DTGS) mid-IR detector was used to acquire ATR-IR spectra. ATR-IR spectra were taken with a resolution of 2 cm^{-1} and 128 scans per spectrum.

3.2.2. X-Ray Powder Diffraction (XRD)

A PANalytical (X'Pert PRO) Multi-Purpose X-Ray diffractometer equipped with a Cu Kα (1.5405 Å) X-Ray source operating at 45 kV/40 mA was used to obtain XRD patterns of the catalysts. The powder samples were analyzed within 10-80° 2θ range using a scan step size of 0.01° and a time per step of 35 s.

3.2.3. BET Specific Surface Area (SSA)

Brunauer, Emmett and Teller (BET) specific surface area (SSA) measurements were executed using a Micromeritics Tristar 3000 surface area and pore size analyzer. With all samples, the filler-rod method, which excludes sample heating, was used.

3.2.4. Transmission Electron Microscopy (TEM) & Energy Dispersive X-Ray Spectroscopy (EDX)

FEI Technai G2F30 transmission electron microscope (TEM) was used to carry out TEM and energy dispersive X-ray (EDX) measurements. The powdered catalysts were dissolved and sonicated in ethanol, followed by drop casting the mixture on carbon-coated copper grids. TEM imaging was carried out in bright-field (BF) conditions.

3.2.5. X-Ray Photoelectron Spectroscopy (XPS)

Thermo Scientific K-Alpha X-ray photoelectron spectrometer (ESCALAB 250) was used to record XPS spectra. Monochromatic Al K_α radiation (1486.6 eV) was used to stimulate photoemission. A pass energy of 200 eV was used for survey scans while high-resolution scans were performed with a 30 eV pass energy. C1s binding energy was set at 284.8 eV for the calibration of the binding energies (B.E.). In survey scans, the number of scans was 2 and that for high-resolution scans were

20. Thermo Avantage software was used in spectra analysis, where smart background was used for background subtraction.

3.2.6. Thermal Gravimetric Analysis (TGA)

In the thermal gravimetric analysis (TGA) measurements, a TA TGA Q500 instrument was used. In TGA experiments, 8.5 mg of the catalyst was heated under 60 mL/min N_2(g) flow from 30°C to 950°C with a linear temperature ramp of 10.0 °C/min.

3.2.7. Nuclear Magnetic Resonance (NMR) Spectroscopy

A Bruker NMR spectrometer was used to record ^{1}H-NMR spectra at 400 MHz and ^{13}C-NMR spectra at 100 MHz. An internal standard (Tetramethylsilane, TMS, 0 ppm) or residual solvent signal (chloroform; at 77.16 ppm for ^{13}C-NMR spectra and at 7.26 ppm for ^{1}H-NMR spectra) were used for the calibrations.

3.3. Catalytic Experiments

3.3.1. Catalytic Aerobic Oxidation of Alkylarenes and Alcohols Experiments

Proper amounts of catalysts (as stated in the activity tables and plots) and 2.0 mL of heptane (solvent) were loaded into a 25-mL Schlenk flask. This flask was filled with 1 bar O_2 (g) and then, 1 bar N_2 (g) for aerobic oxidation experiments in freeze-pump-thaw experiments. Next, the reactor was sealed. The reaction mixture was stirred at 400 rpm in an oil bath at temperatures stated in activity tables and plots for 24 h. Then, they were cooled to room temperature, diluted with ethyl acetate (EtOAc), (except for the 1-phenylethan-1-ol case where dichloromethane (DCM) was used as the diluent), and passed through Celite. Flash column chromatography was used as the purification method with the help of a Silicycle 40-63 μm (230-400 mesh) flash silica gel. The reaction setup used in the liquid phase organic oxidation reactions is presented in **Figure 8**.

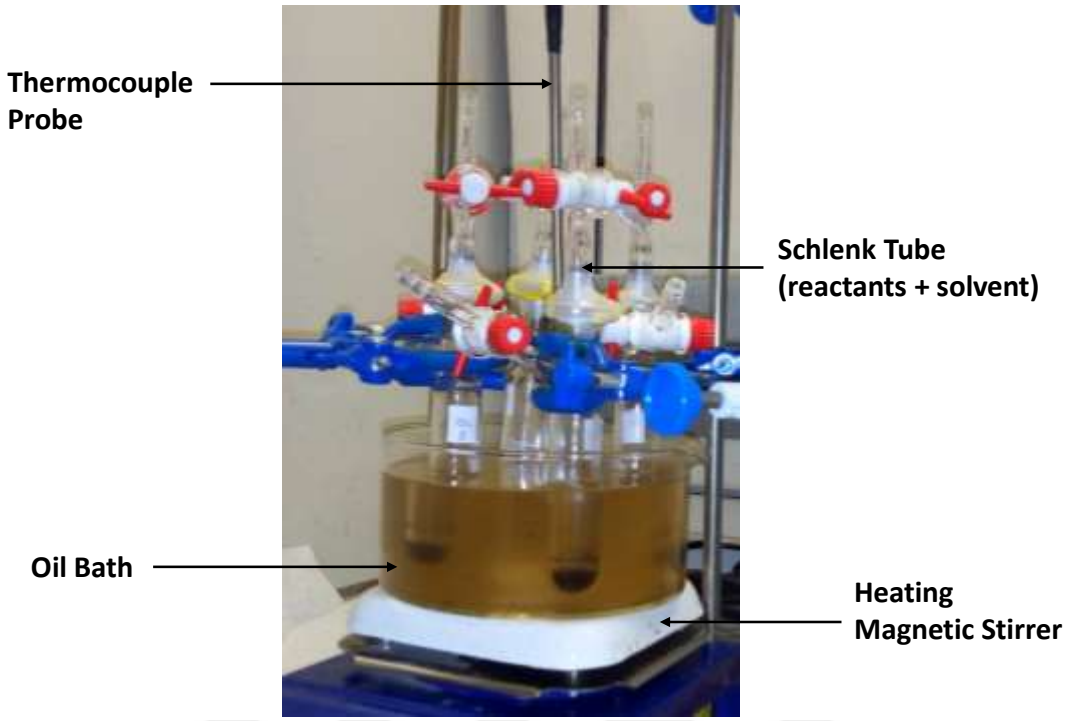

Figure 8. Reaction setup for the catalytic aerobic oxidations of alkylarenes and alcohols to ketones.

3.3.2. Catalytic Carbon Monoxide (CO) Oxidation Experiments

The activities of the catalysts in CO oxidation were measured within a temperature range of 25–300 °C with a linear heating ramp of 5 °C/min under a total pressure of 1 bar. A plug flow reactor equipped with a SRS RGA 200 Quadrupole Mass Spectrometer (QMS) was used to perform flow mode CO oxidation experiments where the gas feed contained 1% CO, 20% O_2 with Ar as the balance gas. In each catalytic CO oxidation test, 300 mg of the catalyst was mixed with 300 mg 60-120 mesh α-Al_2O_3 diluent, which served as a filler for better temperature control in the catalytic bed. A K-type thermocouple inserted in a custom designed quartz rod was inserted into the middle of the catalytic bed to monitor the reaction temperature. The following gas mixtures and gases (all supplied by Linde) were used: Argon (Ar) (>99.99% purity), 2% CO in Ar (CO purity >99.99%), Oxygen (O_2) (>99.99% purity), Hydrogen (H_2) (>99.99% purity). For all CO oxidation reactions, the total flowrate was 500 mL.STP.min^{-1} and the total catalyst and filler volume was 0.5 mL. General view of the plug-flow catalytic reactor used in the catalytic CO oxidation experiments is illustrated in **Figure 9**.

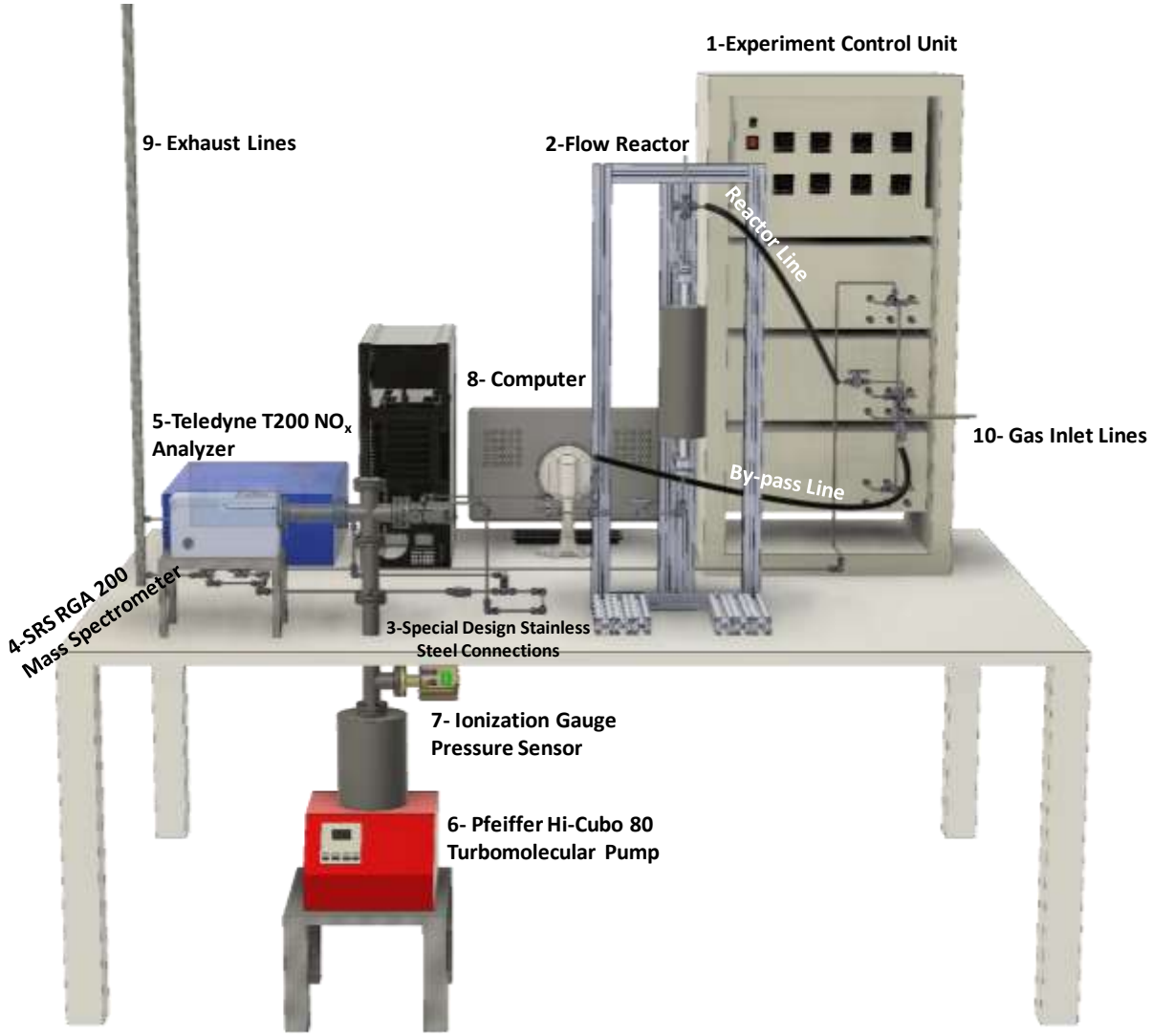

Figure 9. Reaction setup for the catalytic carbon monoxide (CO) oxidation. (Courtesy of Kerem E. Ercan/Ozensoy Research Group)

Thus, the weight hourly space velocity (WHSV) and the gas hourly space velocity (GHSV) parameters used in the catalytic CO oxidation tests were 100 000 $cm^3.STP.g^{-1}.h^{-1}$ and 60 000 h^{-1}, respectively. Catalytic CO oxidation tests were run in the absence (see **Figure 10** for details) and in the presence (see **Figure 11** for details) of a catalyst pretreatment protocol. A standard pretreatment protocol commonly found in the literature was applied for the 1 wt. % Pt/Al_2O_3 commercial benchmark catalyst, (see **Figure 12** for details) for the catalytic CO oxidation studies.

The percentage of converted CO was calculated using the following relationship where $(CO)_{in}$ and $(CO)_{out}$ stand for the CO concentrations in the inlet and the outlet of the reactor:

$$CO\ \%\ conversion = \left|\frac{(CO)_{in} - (CO)_{out}}{(CO)_{in}}\right| X\ 100$$

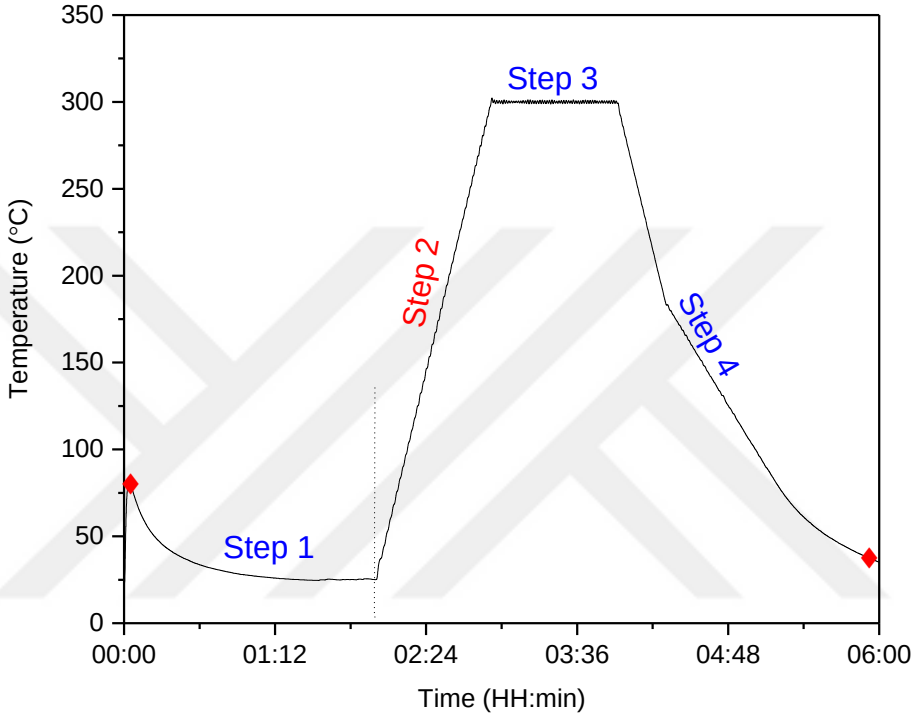

Figure 10. Experimental details of the catalytic CO oxidation tests on metal hydroxide samples in the absence of pretreatment protocol.

Catalytic CO oxidation tests on the metal hydroxide samples in the absence of pretreatment included the following steps:

Step 1: Argon flow at room temperature.

Step 2: Switch to 1% CO and 20% O_2 in Argon (balance) at room temperature and heat the catalyst in this gas mixture with a 5 ^{o}C/min heating ramp up to 300 °C. Note that the catalytic CO oxidation performance data is recorded during this 2nd (i.e., heating) step.

Step 3: Soak at 300 °C for 60 min in the 1% CO and 20% O_2 in Argon (balance) mixture.

Step 4: Cool the catalyst with a 4 ^{0}C/min cooling ramp in the 1% CO and 20% O_2 in Argon (balance) mixture.

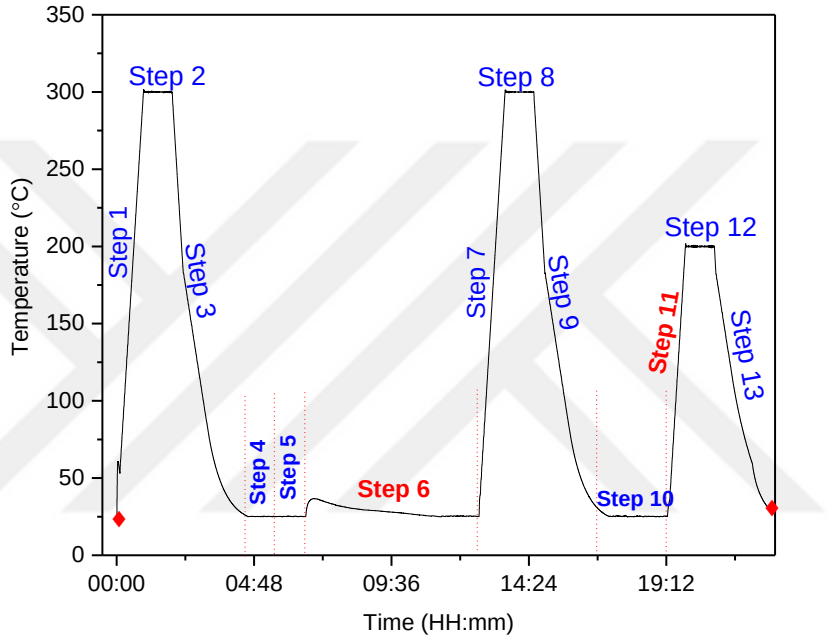

Figure 11. Experimental details of the catalytic CO oxidation tests carried out on metal hydroxide samples using a pretreatment protocol.

Catalytic CO oxidation tests on the metal hydroxide samples in the presence of pretreatment included the following steps:

Step 1: Heat the catalyst in Ar(g) with a 5 ºC/min heating ramp up to 300 °C.

Step 2: Soak the catalyst at 300 °C in Ar(g) for 60 min.

Step 3: Cool the catalyst to room temperature in Ar(g).

Step 4: Switch to Ar(g) at room temperature and purge the catalyst with Ar(g) for 60 min.

Step 5: Switch from reactor line to by-pass line and flow 1% CO and 20% O_2 in Argon (balance) at room temperature. (Purpose is to attain base-line figures for CO and CO_2)

Step 6: Switch from by-pass line to reactor line flow 1% CO and 20% O_2 in Argon (balance) at room temperature. Note that the catalytic room temperature CO oxidation performance data is recorded during the 6^{th} step.

Step 7: Heat the catalyst in Ar(g) with a 5 ºC/min heating ramp up to 300 °C. (Purpose is for catalyst surface regeneration)

Step 8: Soak the catalyst at 300 °C in Ar(g) for 60 min.

Step 9: Cool the catalyst to room temperature in Ar(g).

Step 10: Soak the catalyst at room temperature in Ar(g) for 60 min.

Step 11: Heat the catalyst in 1% CO and 20% O_2 in Argon (balance) with a 5 ^{0}C/min heating ramp up to 200 °C. Note that the catalytic CO oxidation performance data is also recorded during the 11^{th} (i.e., heating) step.

Step 12: Soak the catalyst at 200 °C in 1% CO and 20% O_2 in Argon (balance) for 60 min.

Step 13: Cool the catalyst to room temperature in 1% CO and 20% O_2 in Argon (balance).

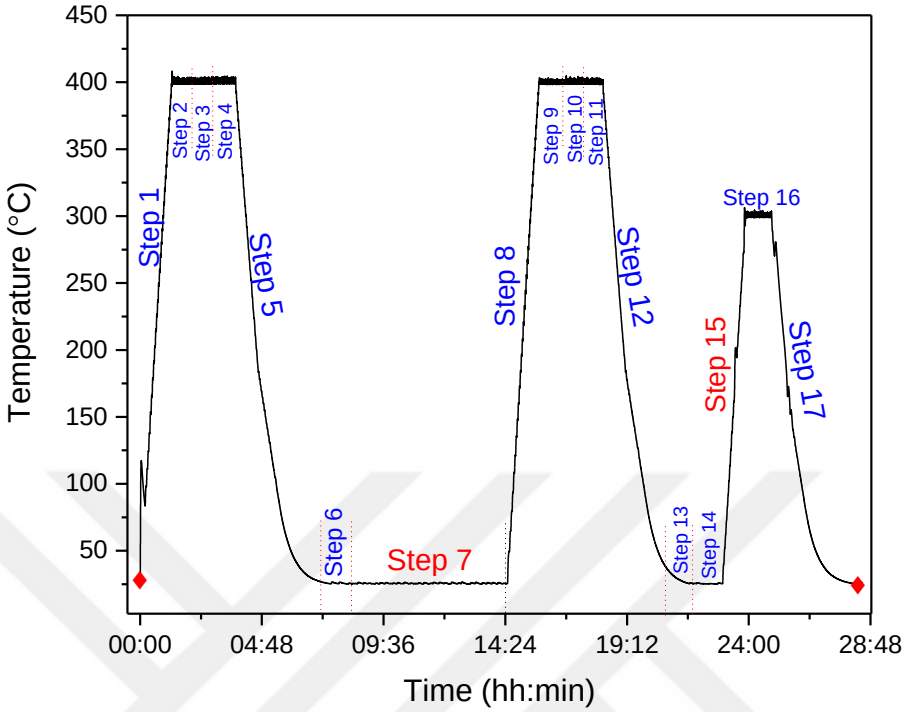

Figure 12. Experimental details of the catalytic CO oxidation tests carried out on 1 wt.% Pt/Al_2O_3 benchmark catalyst using a pretreatment protocol.

Catalytic CO oxidation tests on the 1 wt.% Pt/Al_2O_3 benchmark catalyst in the presence of pretreatment included the following steps:

Step 1: Heat the catalyst in 4 % H_2 (g) balanced with Ar(g) using a 5 ºC/min heating ramp up to 400 °C.

Step 2: Soak the catalyst in 4 % H_2 (g) balanced with Ar(g) at 400 °C for 60 min.

Step 3: Switch to Ar(g) and soak the catalyst at 400 °C for 30 min in Ar(g).

Step 4: Switch to 20 % O_2 in Ar(g) balance and soak the catalyst at 400 °C for 60 min in Ar(g).

Step 5: Cool the catalyst in 20 % O_2 in Ar(g) balance to room temperature with a 4 ºC/min cooling ramp.

Step 6: Switch to Ar(g) at room temperature and purge the catalyst with Ar(g) for 60 min.

Step 7: Switch to 1% CO and 20% O_2 in Argon balance at room temperature. Catalytic performance in this stage is discussed as the low-temperature activity later in the text.

Step 8: Switch to 4 % H_2 (g) balanced and heat the catalyst using a 5 ºC/min heating ramp up to 400 °C.

Step 9: Soak the catalyst in 4 % H_2 (g) balanced with Ar(g) at 400 °C for 60 min.

Step 10: Switch to Ar(g) and soak the catalyst at 400 °C for 30 min in Ar(g).

Step 11: Switch to 20 % O_2 in Ar(g) balance and soak the catalyst at 400 °C for 60 min.

Step 12: Cool the catalyst in 20 % O_2 in Ar(g) balance to room temperature with a 4 ºC/min cooling ramp.

Step 13: Switch to Ar(g) at room temperature and purge the catalyst with Ar(g) for 60 min.

Step 14: Switch to 1% CO and 20% O_2 in Argon balance at room temperature

Step 15: Heat the catalyst to 300 °C with a 5 °C/min heating ramp. This stage is used in the reporting of the catalytic activity.

Step 16: Soak the catalyst in 1% CO and 20% O_2 in Argon balance at 300 °C for 60 min.

Step 17: Cool the catalyst in in 1% CO and 20% O_2 in Argon balance to room temperature with a 4 ºC/min cooling ramp.

CHAPTER 4

4. RESULTS AND DISCUSSION

4.1. Catalytic Oxidation of Organics in Liquid Phase

4.1.1. Catalytic Performance Tests for Xanthene Oxidation to Xanthone on Bimetallic Hydroxides ($Ni_xMn_{1-x}(OH)_2$)

In an attempt to search for an optimized catalyst in xanthene oxidation to xanthone, we performed catalytic performance tests on various bimetallic hydroxides, which were synthesized using various synthetic parameters. As mentioned earlier, influence on three different synthetic parameters on the catalytic performance was investigated: i) type of synthesis method (i.e., solvothermal vs. chemical precipitation), ii) Stoichiometric ratio of Ni/Mn (i.e., nominal relative active metal loading), iii) NaOH concentration. Effect of each of these parameters will be discussed in detail in the forthcoming sections.

4.1.1.1. Influence of the Synthesis Method.

Two major synthesis methods were exploited in the optimization of the $Ni_xMn_{1-x}(OH)_2$ catalysts for aerobic oxidation reactions. Along these lines solvothermal and chemical precipitation methods described in **Sections 3.1.2** above were utilized by keeping Ni/Mn cation ratio constant at a value of 1 (i.e., $Ni_{0.5}Mn_{0.5}(OH)_2$) while also setting the base concentration fixed at [NaOH(aq)] = 3S (i.e., 6.18 M). Xanthene oxidation experiments were carried out as described in **Section 3.3.1**, where the quantitative analysis of reactants remaining after the reaction as well as the products formed was carried out via ^{1}H-NMR spectroscopy. Results of these catalytic activity tests are summarized in **Figure 13**.

In the solvothermal synthesis method (**Figure 6**), two different samples were synthesized by varying the final drying temperature and duration, where in the first sample, drying was performed at 130 °C for 12 h, while in the second sample, it was carried out at 70 °C for 72 h. In the chemical precipitation method, the protocol summarized in **Figure 7** is used. In these catalytic performance tests, 10 mg catalyst was used in each run, where the catalyst was placed inside a Schleck tube containing 0.5 mmol of xanthene dissolved in 2 mL of heptane at 1 bar molecular oxygen.

Figure 13 indicates that the catalyst prepared via the chemical precipitation method significantly outperforms the catalysts prepared using the solvothermal method. Thus, in the rest of the study, chemical precipitation method was preferred and the influence of the remaining synthetic parameters were investigated.

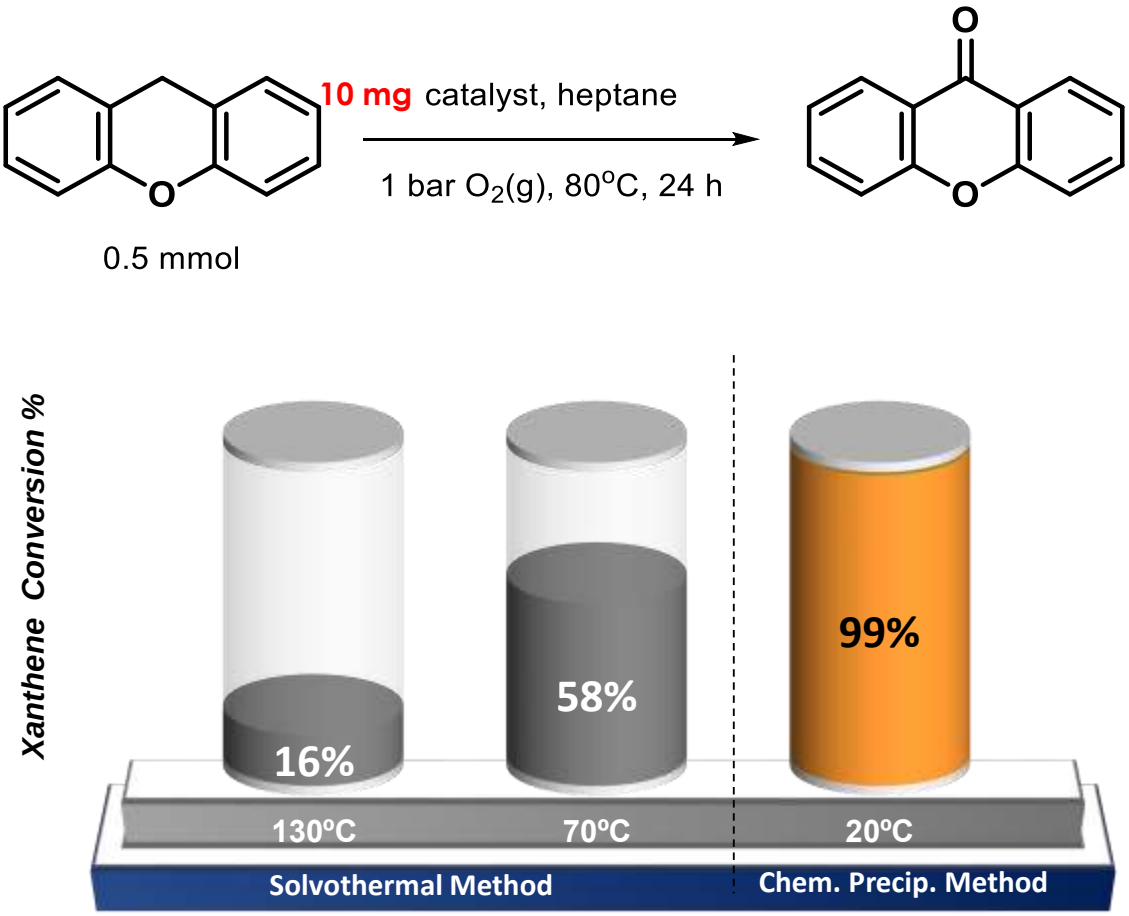

Figure 13. Catalytic activity data for $Ni_{0.5}Mn_{0.5}(OH)_2$ catalysts prepared via solvothermal and chemical precipitation methods in the aerobic oxidation of xanthene to xanthone. S stands for the stoichiometric NaOH(aq) concentration (i.e., 2.06 M).

4.1.1.2. Influence of the Relative Active Metal Loading

In an attempt to find the optimal metal precursor loading for the $Ni_xMn_{1-x}(OH)_2$ catalyst, varying amounts of nickel and manganese precursors were used (**Table 2**) in the chemical precipitation

protocol, while keeping the NaOH concentration at 6S. NaOH concentration of 6S was used rather than 3S to utilize hydroxide anions in excess cation charge compensation. Hence, reducing the amount of chloride anions that get intercalated for excess cation charge compensation. Since the catalytic xanthene conversion % values could be significantly increased by modifying the Ni/Mn ratio in the catalysts, a smaller amount of catalyst (i.e., 5 mg) was used in this set of catalytic performance tests.

It can be seen in **Figure 14** that monometallic hydroxides i.e., $Mn(OH)_2$ and $Ni(OH)_2$ exhibit the lowest xanthene conversions of 4% and 7%, respectively. Interestingly, incorporation of only 0.05% Mn active sites to the monometallic $Ni(OH)_2$ hydroxide structure leads to a drastic boost in xanthene conversion, where the activity increases by more than 5-fold for $Ni_{0.95}Mn_{0.05}(OH)_2$. This important observation implies that a synergistic interaction exists between Ni and Mn sites in bimetallic $Ni_xMn_{1-x}(OH)_2$ hydroxides, where the electronic, catalytic and chemical properties of these nanomaterials can be fine-tuned by modifying the relative metal loadings of different active metal cations. **Figure 14** also reveals a typical volcano-type plot revealing an optimum relative metal cation loading ratio, where the maximum catalytic activity in xanthene oxidation is observed for $Ni_{0.6}Mn_{0.4}(OH)_2$.

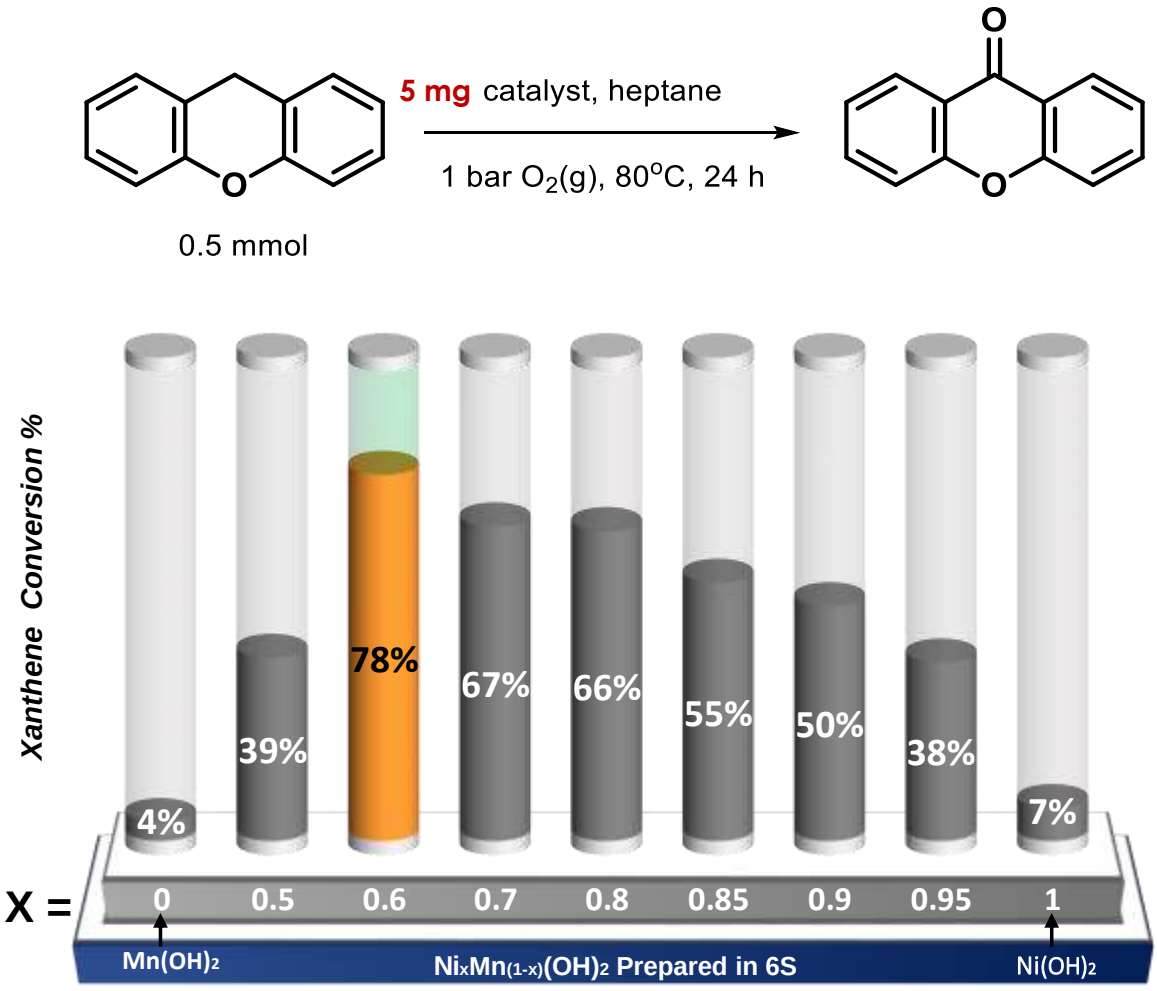

Figure 14. Catalytic activity data for $Ni_xMn_{1-x}(OH)_2$ catalysts in the aerobic oxidation of xanthene to xanthone. Catalysts were prepared via chemical precipitation method using various Ni and Mn precursor amounts and a NaOH(aq) concentration of 6S. S stands for the stoichiometric NaOH concentration (i.e., 2.06 M).

4.1.1.3. Influence of NaOH Concentration.

After determining the optimized synthesis method and the optimum metal precursor loadings, the final optimization set focused on the effect of NaOH(aq) concentration used in the synthesis. In this optimization set, the best catalyst in the previous two optimization sets (i.e., $Ni_{0.6}Mn_{0.4}(OH)_2$ synthesized via chemical precipitation method) was synthesized using various NaOH(aq) concentrations. **Figure 15** illustrates the corresponding catalytic xanthene oxidation activity test

results. As can be seen in **Figure 15,** extremely low or extremely high NaOH(aq) concentrations lead to limited xanthene oxidation activities, where the catalytic performance is maximized for 9S (S stands for the stoichiometric NaOH(aq) concentration of 2.06 M).

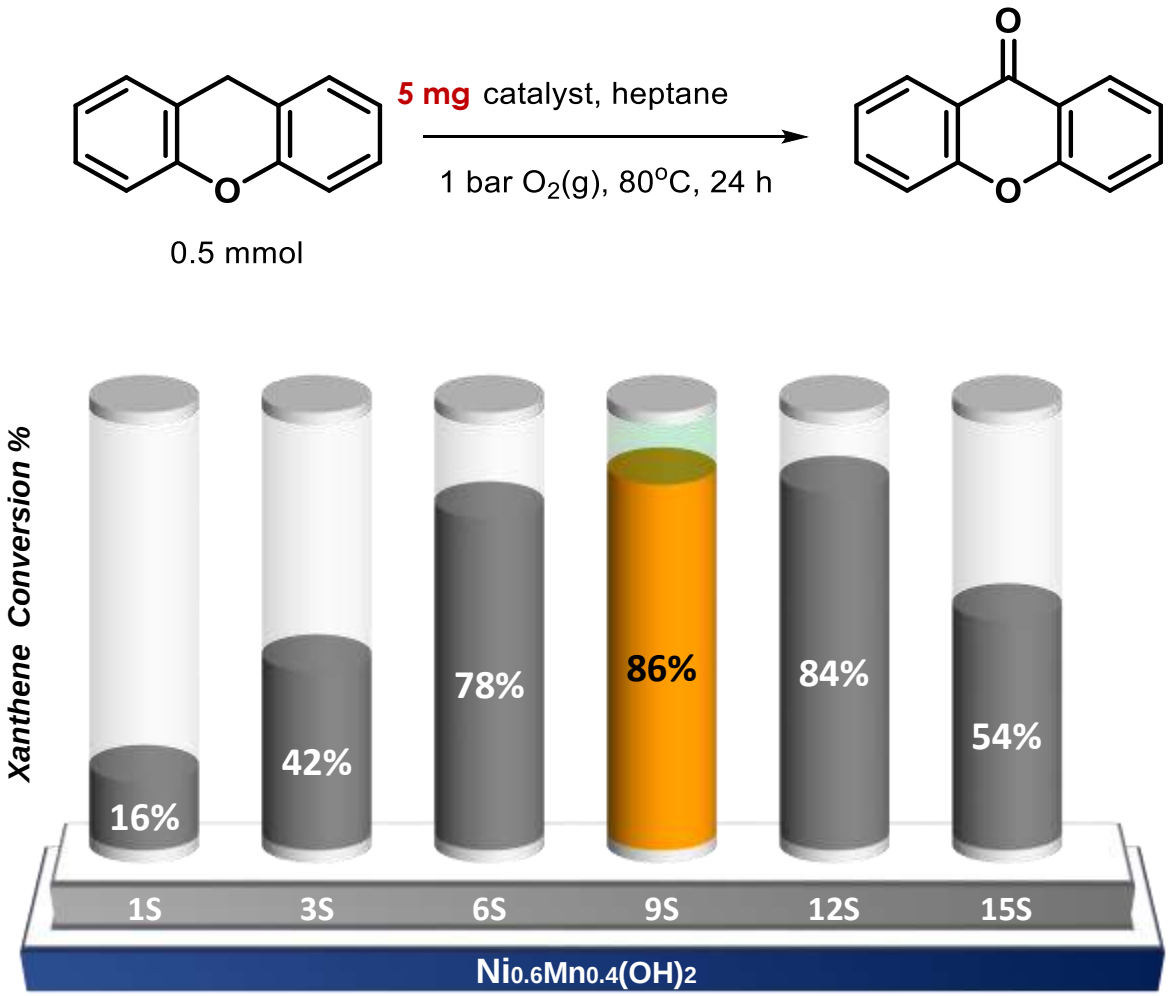

Figure 15. Catalytic activity data for $Ni_{0.6}Mn_{0.4}(OH)_2$ catalysts in the aerobic oxidation of xanthene to xanthone. Catalysts were prepared via chemical precipitation method using various NaOH(aq) concentrations. S stands for the stoichiometric NaOH concentration (i.e., 2.06 M).

4.1.2. Catalytic Performance Data for the Heterogeneous Aerobic Oxidation of Xanthene to Xanthone Present in the Literature

Heterogeneous catalytic aerobic oxidation of xanthene to xanthone was investigated in various studies in the literature. [47-66] **Figure 16** illustrates a graphical compilation of the data given in **Table 1** where the results were normalized to 0.5 mmol xanthene (as the starting material) for easy comparison.

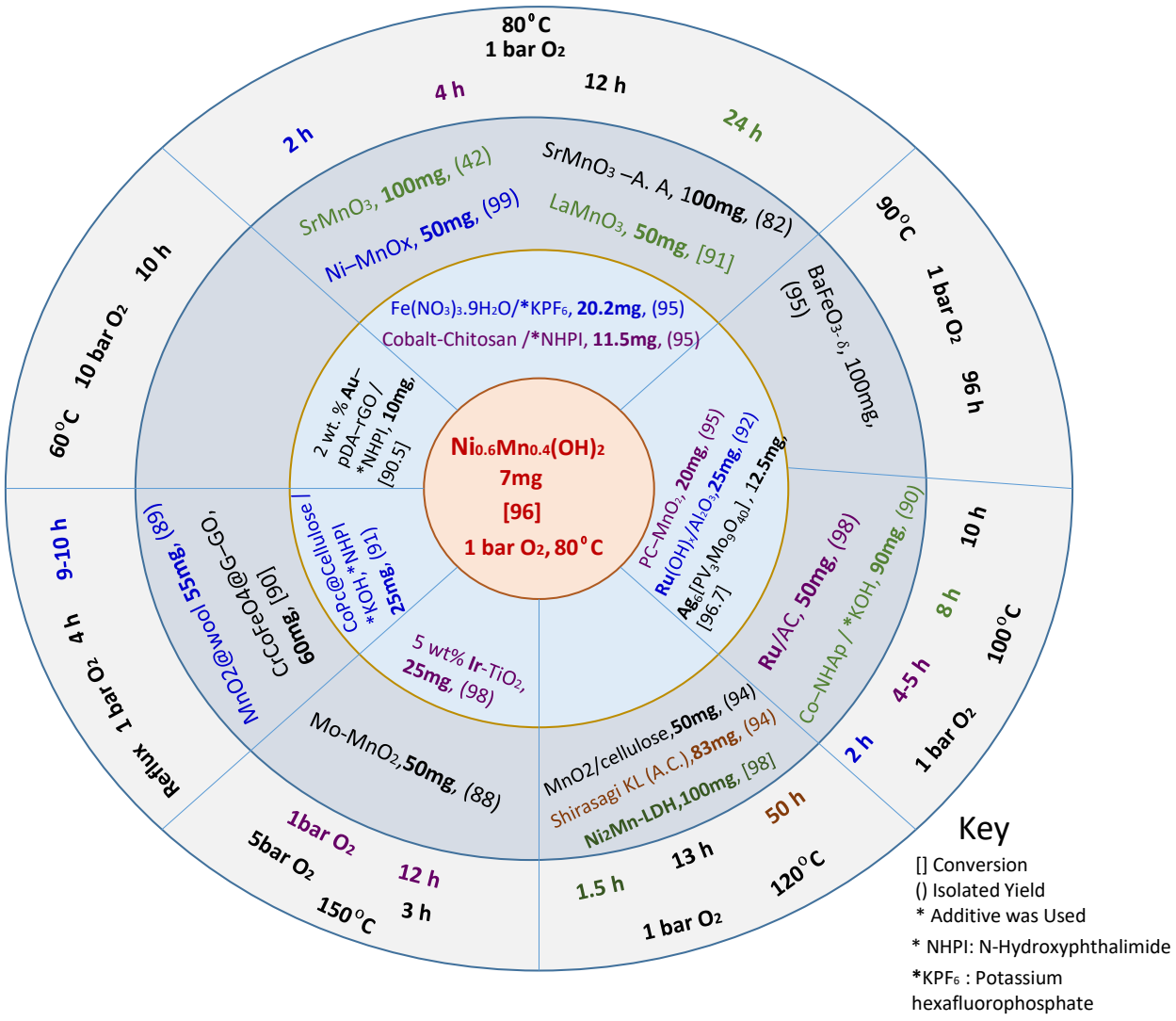

Figure 16. Graphical compilation of the literature data given in Table 1 for the heterogeneous catalytic aerobic oxidation of xanthene to xanthone. Note that the catalyst amounts were normalized to 0.5 mmol substrate (i.e., xanthene) amount. Chemicals with (*) correspond to external additives included in the reaction mixture to boost catalytic performance. References for the catalysts can be found in **Table 1**.

In **Figure 16**, catalytic performance values reported in the literature are illustrated using a circular hierarchy, where the catalysts in the outer regions are less active (in terms of per gram of catalyst used for a given activity %), while the catalysts in the inner circles are more active. The bull's eye (i.e., the center) represents the most active catalyst in the literature (which is the optimized catalyst reported in the current work, i.e., $Ni_{0.6}Mn_{0.4}(OH)_2$-9S. The outermost circle lists different reaction conditions (e.g., reaction duration, O_2 pressure, and temperature) used in different studies. The region between the 2nd and the 3rd circles from the center lists typically PGM-free catalysts, while the region between the 1st and the 2nd circles list the PGM-containing catalysts.

Figure 16 clearly indicates that $Ni_{0.6}Mn_{0.4}(OH)_2$-9S catalyst developed in the current work outperforms all of the PGM-containing and PGM-free catalysts in the literature by yielding 96% xanthene conversion using the lowest catalyst amount (i.e., 7 mg) at the lowest O_2 pressure (i.e., 1 bar) and at one of the lowest reaction temperatures (i.e., 80 °C). Furthermore, $Ni_{0.6}Mn_{0.4}(OH)_2$-9S catalyst can offer 96% xanthene conversion within a short reaction duration of 12 h, suggesting a an extremely fast kinetics as compared to the existing catalysts in the literature. Furthermore, unlike some of the high performing catalysts given in **Figure 16,** which require inclusion of various additives, promoters, or performance boosters (labeled with * in **Figure 16**), $Ni_{0.6}Mn_{0.4}(OH)_2$-9S catalyst does not require the use of any additives rendering it economically and ergonomically the most preferable catalyst. In some other cases, high performance was obtained by refluxing of the solvent, which is also not required for $Ni_{0.6}Mn_{0.4}(OH)_2$-9S.

It should also be emphasized that in one of our very recently published studies (Y. Şahin, A. T. Sika-Nartey, E. Ozensoy, and Y. E. Türkmen et al. ACS Applied Materials & Interfaces, 2021, accepted in press, Ref 51), we reported a highly active $LaMnO_3$ perovskite catalyst, where the 91 % xanthene conversion achieved with 50 mg of $LaMnO_3$ in 24 h can now be achieved using only 7 mg $Ni_{0.6}Mn_{0.4}(OH)_2$-9S catalyst in 12 h under same reaction conditions. Therefore, it is clear the currently reported precious metal-free $Ni_{0.6}Mn_{0.4}(OH)_2$-9S mixed metal hydroxide catalyst provides an order of magnitude improvement in the amount (mass) of catalyst needed for >90 % xanthene conversion.

4.1.3. Demonstration of the Wide Utility of $Ni_{0.6}Mn_{0.4}(OH)_2$-9S Catalyst in the Aerobic Oxidation of Other Alkylarenes to Ketones.

In order to demonstrate that the extraordinary catalytic activity of the $Ni_{0.6}Mn_{0.4}(OH)_2$-9S catalyst developed in the current work is not only limited to the oxidation of xanthene, we tested this catalyst in the aerobic oxidation of other alkylarenes. Furthermore, to prove the catalytic power of the $Ni_{0.6}Mn_{0.4}(OH)_2$-9S catalyst, we chose substrates (i.e., reactants) with increasing homolytic bond dissociation energy (BDE). [75 -78] Typically, catalytic oxidation of substrates with higher homolytic BDE can be more challenging.

Thus, **Table 3** lists the catalytic oxidation tests with the $Ni_{0.6}Mn_{0.4}(OH)_2$-9S catalyst on the substrates which produced successful results, while **Table 4** shows the data for the substrates which yielded unsuccessful results (due to low catalytic activity or due to other technical issues concerning product and solvent separation). For all reactions, the reaction duration was 24 h, the solvent was n-heptane, and the molecular oxygen (O_2) pressure was fixed at 1 bar. Both tables report the corresponding catalyst amount and the reaction temperature for each entry. **Table 3** shows that, as the catalytic oxidation becomes more challenging with increasing homolytic BDE of the substrate, use of higher reaction temperatures and greater catalyst amounts were required for such substrates.

In overall, **Table 3** verifies that the superior catalytic oxidation capability and high selectivity of the $Ni_{0.6}Mn_{0.4}(OH)_2$-9S catalyst is not only limited to xanthene and it can be used in the selective oxidation of a wide variety of other alkylarene substrates in a successful and efficient manner.

Table 3. Successful attempts of catalytic aerobic oxidation of various alkylarenes to ketones using $Ni_{0.6}Mn_{0.4}(OH)_2$-9S. For all reactions, the duration was 24 h and the solvent was n-heptane. [a] Homolytic Bond Dissociation Energy (B.D.E.) of the reactant organic compounds.

Name & Structure	Product	Catalyst Amount (mg)	Rxn Temperature (°C)	Conversion %	Selectivity Ketone / Alcohol	Homolytic BDE (kcal/mole) [a]
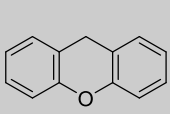 xanthene	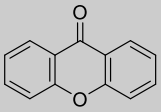 xanthone	7	80	> 99	100/0	80.7
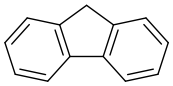 fluorene	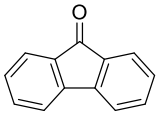 fluorenone	20	80	>99	100/0	82.0
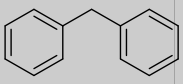 diphenylmethane	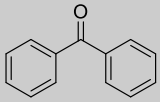 benzophenone	20	110	92	100/0	84.5
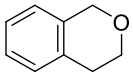 isochroman	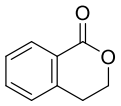 isochromanone	20	110	96	100/0	-

Table 4 shows a substrate scope for the unsuccessful attempts of catalytic oxidation using $Ni_{0.6}Mn_{0.4}(OH)_2$-9S. Adamantane and *cis*-decalin have relatively high homolytic B.D.E. and hence the reaction temperature was increased to 150 °C. Due to this, the solvent had to be changed from n-heptane (since it was not stable at that temperature) to n-decane. In both cases 30 mg catalyst amount was used. After 24 h of reaction, a brown color was observed in the reaction medium indicating the formation of products in both cases. However, due to the limited volatility of n-decane, the product(s) could not be isolated even under vacuum conditions for multiple days. Further studies are ongoing to isolate the products from n-decane medium. For the aerobic oxidation of menthol and indan, no reaction was detected at 80 °C and 110 °C, respectively. However, we believe that harsher reaction conditions (such as 150 °C) may yield successful results. Such experiments will be carried out after resolving the n-decane volatility issue.

Table 4. Unsuccessful attempts of catalytic aerobic oxidation of alkylarenes to ketones using $Ni_{0.6}Mn_{0.4}(OH)_2$-9S. For all reactions, the duration was 24 h and the solvent was n-heptane unless otherwise specified. [a] Homolytic Bond Dissociation Energy (B.D.E.) of the reactant organic compounds.

Name & Structure	Product	Catalyst Amount (mg)	Rxn Temperature (°C)	Conversion %	Homolytic BDE (kcal/mole) [a]
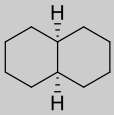 cis-decalin	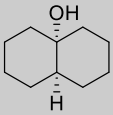 cis-decalol	30	150	- n-decane: volatility problem	-
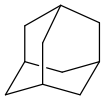 adamantane	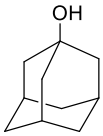 adamantanol	30	150	n-decane: volatility problem	98.5
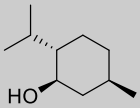 menthol	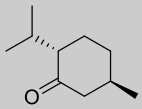 menthone	20	80	No Reaction	-
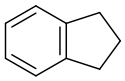 indan	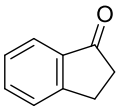 indanone	20	110	No Reaction	85.9

4.1.4. Demonstration of the Wide Utility of $Ni_{0.6}Mn_{0.4}(OH)_2$-9S Catalyst in the Aerobic Oxidation of Alcohols to Ketones.

Additionally, to test the effectiveness of the optimized $Ni_{0.6}Mn_{0.4}(OH)_2$-9S catalyst towards a different set of organic substrate scope, two different alcohol substrates were considered with different homolytic B.D.E. As illustrated in **Table 5**, optimized $Ni_{0.6}Mn_{0.4}(OH)_2$-9S catalyst showed a superior activity towards the catalytic aerobic oxidation of both diphenylmethanol and 1-phenylethan-1-ol.

Table 5. Successful attempts of catalytic aerobic oxidation of alcohols to ketones using $Ni_{0.6}Mn_{0.4}(OH)_2$-9S. For all reactions, the duration was 24 h and the solvent was n-heptane. [a] Homolytic Bond Dissociation Energy (B.D.E.) of the reactant organic compounds.

Name & Structure	Product	Catalyst Amount (mg)	Rxn Temperature (°C)	Conversion %	Homolytic BDE (kcal/mole) [a]
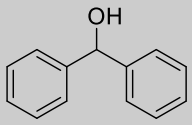 diphenylmethanol	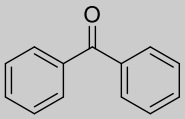 benzophenone	10	80	> 99	75.4
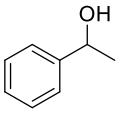 1-phenylethan-1-ol	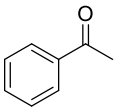 acetophenone	30	80	> 99	88.3

4.2. Characterization and Spectroscopic Studies

In the previous sections, we demonstrated that mixed metal hydroxide systems can be synthetically fine-tuned in order to optimize their catalytic oxidation activity and selectivity toward a wide variety of alkylarenes and alcohols. In this section, we will provide experimental results to shed light on the structural origins of the enhanced catalytic performance of these novel catalytic systems. Along these lines, structure of this novel nanomaterial architecture was studied using a

multitude of characterization techniques including ATR-IR, XRD, BET-SSA, TGA, TEM, EDX, and XPS.

4.2.1. Vibrational Structural Analysis via Attenuated Total Reflectance – Infrared (ATR-IR) Measurements

Bode et. al. reported that two different pseudopolymorphs of $Ni(OH)_2$ exist (α-phase and β-phase). [13] One of the efficient methods to identify these different phases involves vibrational spectroscopy. Particularly, ATR-IR investigation of the -OH spectroscopic features within 3000-4000 cm^{-1} can be useful to distinguish between the different $Ni(OH)_2$ pseudopolymorphs (**Figure 17**). This is mostly due to the fact that while the α-phase has incorporated water molecules which are H-bonded to each other resulting in the observation of a broad and a convoluted vibrational signature within 3000-3600 cm^{-1}. In contrast, β-phase contains isolated hydroxide functionalities yielding sharp and blue-shifted vibrational peaks at >3500 cm^{-1}. Obviously, $Ni(OH)_2$ structures containing both α and β-phases reveal a combination of these aforementioned -OH vibrational signatures (**Figure 17**).

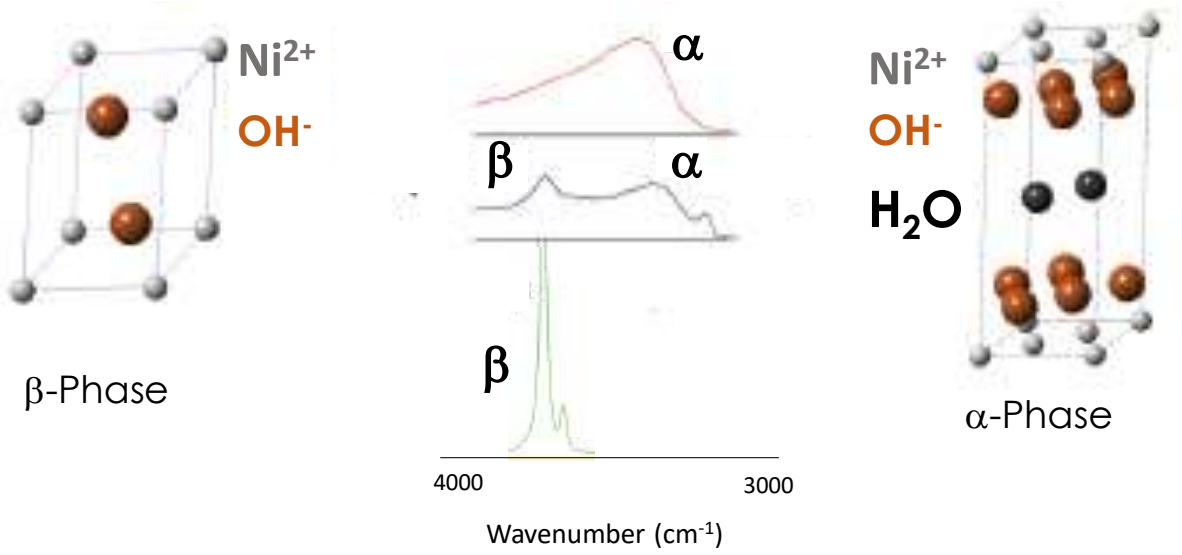

Figure 17. Typical -OH vibrational features observed in ATR-IR spectroscopy for different phases nickel hydroxides. [79]

Low frequency region (i.e., features located below < 1400 cm^{-1} as well as their overtones at higher frequencies) of the ATR-IR spectra of metal hydroxides (**Figure 18**) can also be highly informative, as they reflect well-known characteristic vibrational features associated with particular lattice phonons which are due to the concerted oscillations of metal cations and hydroxide ions throughout the entire solid (e.g., A1g + acoustic mode, E_g + A_{2u} (TO), E_g+E_u (TO) modes etc.). [79] Note that the optical components of the ATR-IR spectrometer used in the current work included a diamond ATR crystal with a low frequency cut-off at 100 cm^{-1} and a KBr beam splitter with a low frequency cut-off at 350 cm^{-1}. Thus, the lowest achievable frequency that can be safely measured in the current ATR-IR spectra was ca. 400 cm^{-1} that allowed confident analysis of the low frequency metal hydroxide phonons. In addition to these features, within 1200-1000 cm^{-1} E_u (LO) O−H bending modes were also visible due to the hydroxide ions in the metal hydroxide structure. [79]

Figure 18 shows the ATR-IR spectra for $Ni_xMn_{1-x}(OH)_2$ catalysts used in the aerobic oxidation of xanthene to xanthone. These catalysts were prepared via chemical precipitation method using various Ni and Mn precursor amounts and a NaOH(aq) concentration of 6S. It is apparent that while pure $Ni(OH)_2$ (x = 1) reveals a β-$Ni(OH)_2$ structure, pure $Mn(OH)_2$ (x = 0) shows a α-$Mn(OH)_2$ structure. On the other hand, $Ni_{0.6}Mn_{0.4}(OH)_2$ which is the most active mixed metal hydroxide catalyst in this series exhibits a predominantly α-phase where a minor contribution from β-phase cannot be ruled out. It is important to emphasize that the ATR-IR data given in Figure **18** clearly indicate that the structure of the mixed metal hydroxides can be accurately fine-tuned by modifying the Ni/Mn cation content.

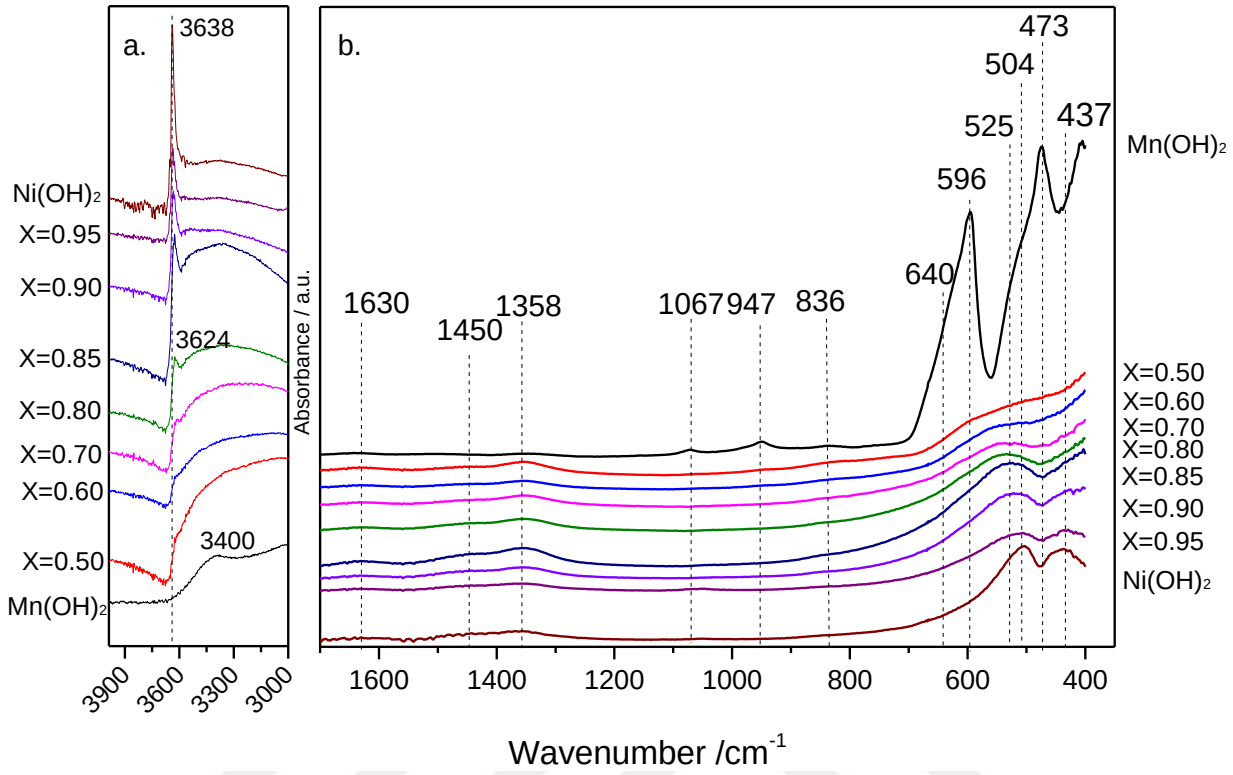

Figure 18. ATR-IR spectra for $Ni_xMn_{1-x}(OH)_2$ catalysts. Catalysts were prepared via chemical precipitation method using various Ni and Mn precursor amounts and a NaOH(aq) concentration of 6S. S stands for the stoichiometric NaOH concentration (i.e., 2.06 M).

Figure 18 presents the ATR-IR spectra for $Ni_xMn_{1-x}(OH)_2$ catalysts prepared via chemical precipitation method using various Ni and Mn precursor amounts and a NaOH(aq) concentration of 6S. It can be inferred from **Figure 18** that, $Ni_xMn_{1-x}(OH)_2$ synthesized with NaOH(aq) concentrations of 6S, where $0 \leq x \leq 0.7$ predominantly exhibit α-phase. On the other hand, higher Ni precursor amounts, i.e. $0.8 \leq x \leq 0.95$ leads to the presence of both α and β-phases. And $Ni(OH)_2$ exhibit only β-phases. The lowest frequency peaks at 437 and 473 cm^{-1} in **Figure 18b** can be attributed to typical "*$A1_g$ + acoustic mode*" combination signals of metal hydroxides, while the next set of slightly higher frequency features at 504, 525, and 596 cm^{-1} can be assigned to $E_g + A_{2u}$ (TO) or $E_g + E_u$ (TO) combination modes of metal hydroxides. [79] The weak feature at 836 cm^{-1} can also be tentatively assigned to MnOOH minority species. [107] Bands at 947 and 1067 cm^{-1} are ascribed to E_u (LO) O−H bending modes of metal hydroxides. [79] Vibrational signatures at 1358

and 1450 cm^{-1} are due to E_g + A_{2u} (TO) combination bands.[79] Finally, the peak at 1630 cm^{-1} is associated with adsorbed water molecules on the surface. [79]

Figure 19 presents the ATR-IR spectra for $Ni_{0.6}Mn_{0.4}(OH)_2$ catalysts prepared via chemical precipitation method using various NaOH(aq) concentrations. It can be inferred from **Figure 19** that, $Ni_{0.6}Mn_{0.4}(OH)_2$ synthesized with NaOH(aq) concentrations of 1S, 3S and 6S predominantly exhibit α-phase. On the other hand, higher concentrations of NaOH(aq) leads to the presence of both α and β-phases. Thus, it is clear that the ultimately optimized xanthene oxidation catalyst $Ni_{0.6}Mn_{0.4}(OH)_2$-9S contains both α and β-phases. Same peak assignments made in **Figure 18** can be made here. A detailed ATR-IR spectrum of the optimized $Ni_{0.6}Mn_{0.4}(OH)_2$-9S catalyst is also given in **Figure 20**.

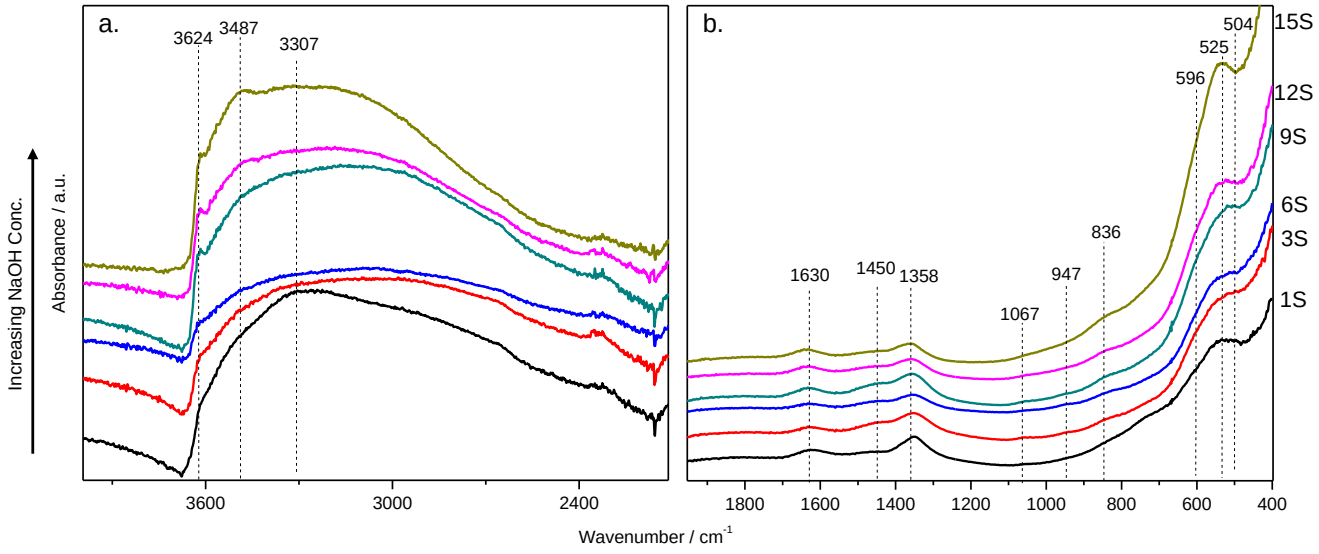

Figure 19. ATR-IR spectra for $Ni_{0.6}Mn_{0.4}(OH)_2$ catalysts. Catalysts were prepared via chemical precipitation method using various NaOH(aq) concentrations. S stands for the stoichiometric NaOH concentration (i.e., 2.06 M).

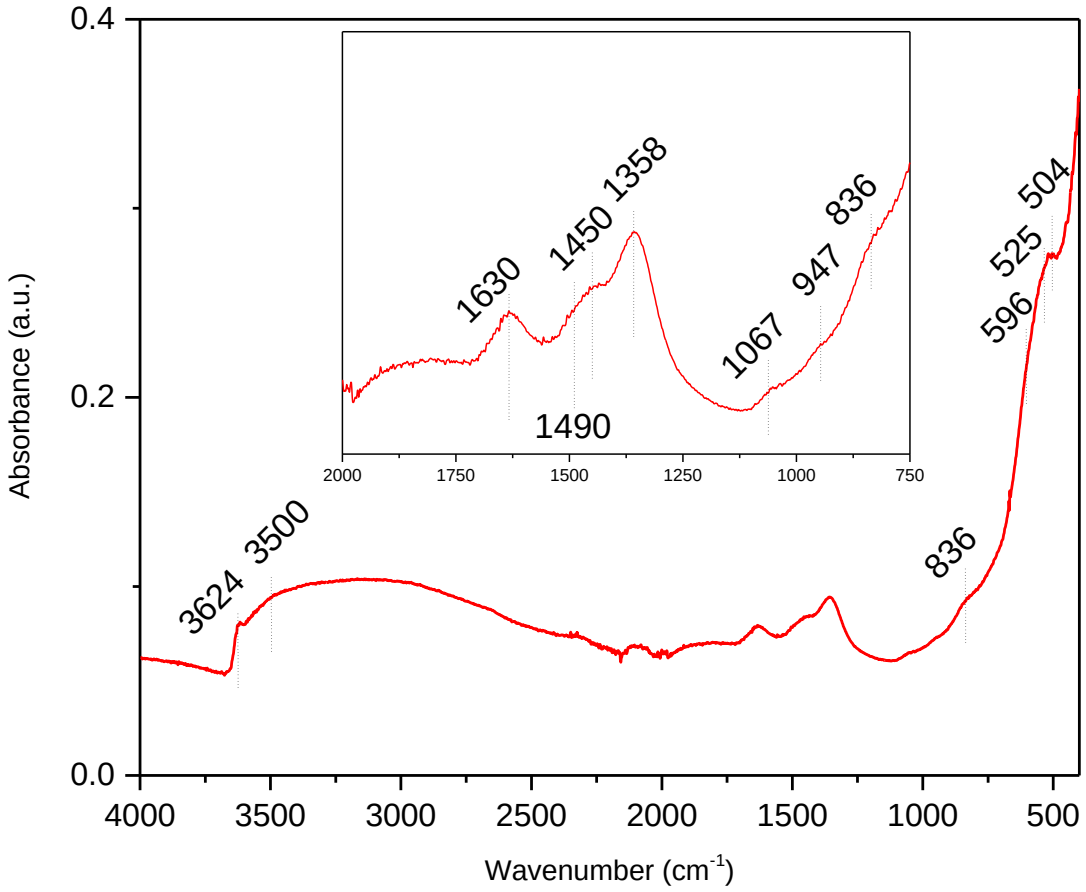

Figure 20. ATR-IR spectra for $Ni_{0.6}Mn_{0.4}(OH)_2$-9S catalyst prepared via chemical precipitation method S stands for the stoichiometric NaOH concentration (i.e., 2.06 M).

4.2.2. Analysis of the Crystal Structure via X-Ray Diffraction (XRD) Measurements

XRD data acquired from metal hydroxide systems can reveal the type of structural disorders within the crystal structure. Stacking fault disorders (**Figure 4**) and α/β-interstratifications (**Figure 5**) were reported to have an impact on the measured XRD peaks. [12] Strong intra-layer interactions between ions within the layered double hydroxide sheets along with the relatively weak inter-layer interactions between these layers cause stacking faults in these systems. Rotational faults result in selective line broadening in XRD peaks as it occurs along the direction of the crystallographic *c*-axis. However, in the case of the presence of α/β-interstratifications, XRD peaks appear even further shifted and broadened. [12, 32]

Figure 21 shows the effect of metal precursor loading on the crystal structure of $Ni_xMn_{(1-x)}(OH)_2$ samples synthesized with a NaOH(aq) concentration of 6S. It can be seen that the diffraction signal at ca. $2\theta = 18.6°$ in **Figure 21b** reveals increasing broadening with increasing Ni content in the crystal structure. This peak broadening can be attributed to rotational stacking faults. **Figure 21b-c** indicate that for $0.5 \leq x \leq 0.7$, no apparent peak shifts were observed in the XRD features, while peak broadening continues to exist. For x values of 0.8 to 0.95, peak shifts are clearly visible. In light of these observations, it can argued that $Ni_{0.5}Mn_{0.5}(OH)_2$, $Ni_{0.6}Mn_{0.4}(OH)_2$ and $Ni_{0.7}Mn_{0.3}(OH)_2$ synthesized with a NaOH(aq) concentration of 6S exhibit the α-phase. However, $Ni_{0.8}Mn_{0.2}(OH)_2$, $Ni_{0.85}Mn_{0.15}(OH)_2$, $Ni_{0.9}Mn_{0.1}(OH)_2$ and $Ni_{0.95}Mn_{0.05}(OH)_2$ reveal both α and β-phases. It should be noted that these XRD assignments are in good agreement with the ATR-IR data (**Figure 18**) discussed in the former section.

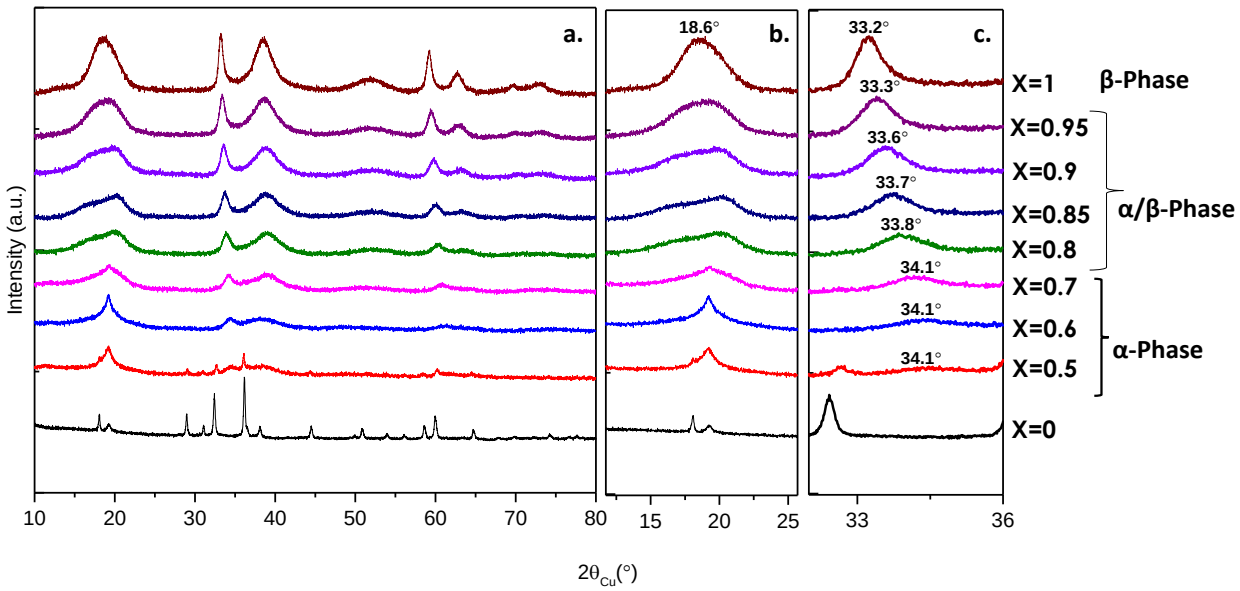

Figure 21. XRD data for $Ni_xMn_{1-x}(OH)_2$ catalysts. Catalysts were prepared via chemical precipitation method using various Ni and Mn precursor amounts and a NaOH(aq) concentration of 6S. S stands for the stoichiometric NaOH concentration (i.e., 2.06 M).

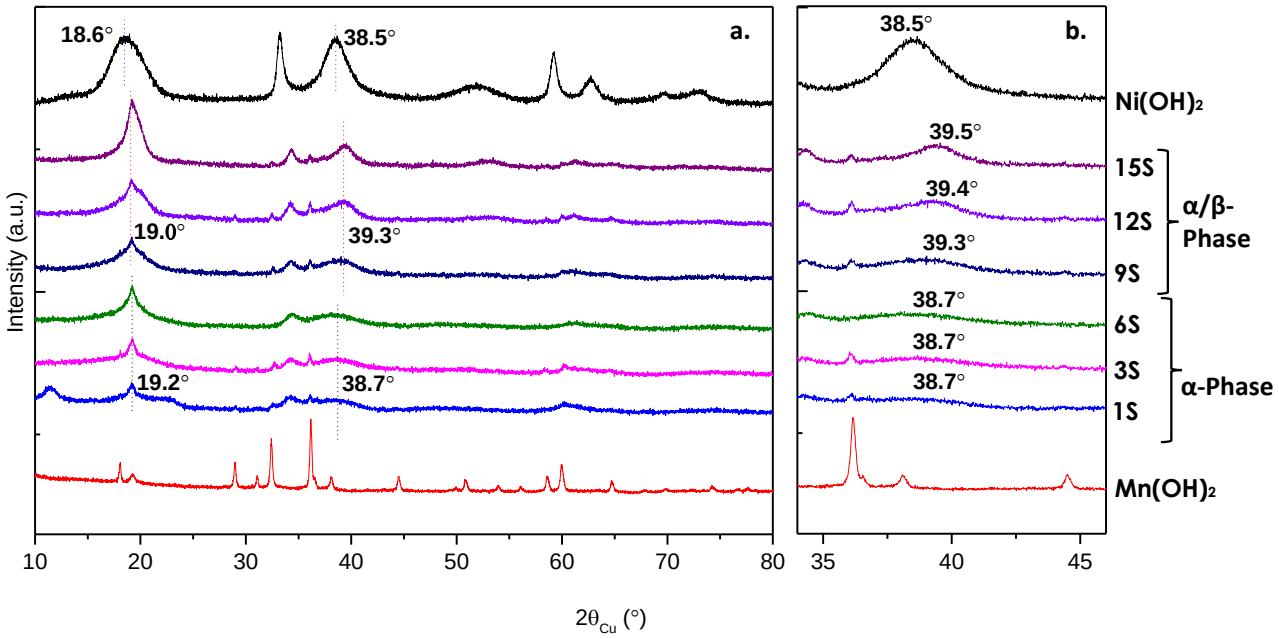

Figure 22. XRD data for $Ni_{0.6}Mn_{0.4}(OH)_2$ catalysts. Catalysts were prepared via chemical precipitation method using various NaOH(aq) concentrations. S stands for the stoichiometric NaOH concentration (i.e., 2.06 M).

Figure 22b shows that $Ni_{0.6}Mn_{0.4}(OH)_2$ synthesized with NaOH(aq) concentrations of 1S, 3S, and 6S exhibit peak broadening around 38.7° without any discernible peak shifts. Such broadening can be ascribed to the presence of rotational faults in the crystal structure. However, corresponding samples synthesized with NaOH(aq) concentrations of 9S, 12S, and 15S reveal peak shifts within the ranges of 39.2° to 39.6°. These peak shifts are attributed to α/β interstratifications. Hence, it is apparent that the ultimately optimized $Ni_{0.6}Mn_{0.4}(OH)_2$-9S catalyst for xanthene oxidation contains rotational faults as well as α/β interstratification structural disorders.

4.2.3. Specific Surface Area Analysis via BET Measurements

Figure 23 shows the BET SSA measurements for $Ni_xMn_{1-x}(OH)_2$ catalysts with various Ni/Mn ratios synthesized with a NaOH(aq) concentration of 6S. It is seen that $Mn(OH)_2$ possesses the lowest BET SSA value of 24 m^2/g, while $Ni(OH)_2$ has the highest BET SSA value of 179 m^2/g. It is seen that increasing Ni content in the mixed metal hydroxide structure typically increases the SSA value. For a NaOH(aq) concentration of 6S, the best catalyst showing the highest xanthene oxidation activity is $Ni_{0.6}Mn_{0.4}(OH)_2$ with a SSA of 120 m^2/g. Data given in **Figure 23** point out to the fact that SSA is not the foremost structural property governing the ultimate catalytic reactivity since the catalyst with the highest SSA of 179 m^2/g (i.e., $Ni(OH)_2$-6S) has a lower activity than that of $Ni_{0.6}Mn_{0.4}(OH)_2$-6S.

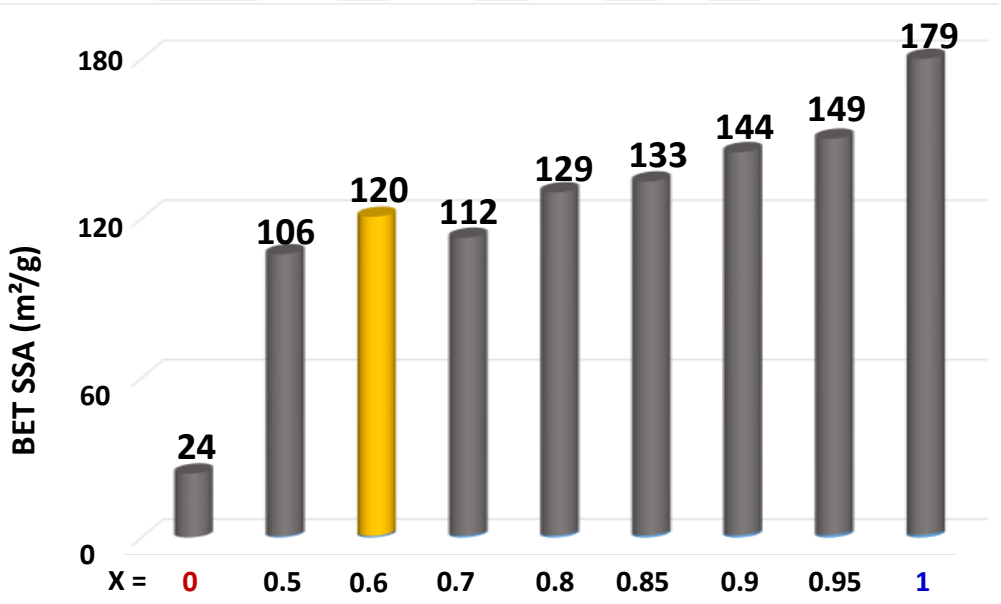

Figure 23. BET SSA values for $Ni_xMn_{1-x}(OH)_2$ catalysts. Catalysts were prepared via chemical precipitation method using various Ni and Mn precursor amounts and a NaOH(aq) concentration of 6S. S stands for the stoichiometric NaOH concentration (i.e., 2.06 M).

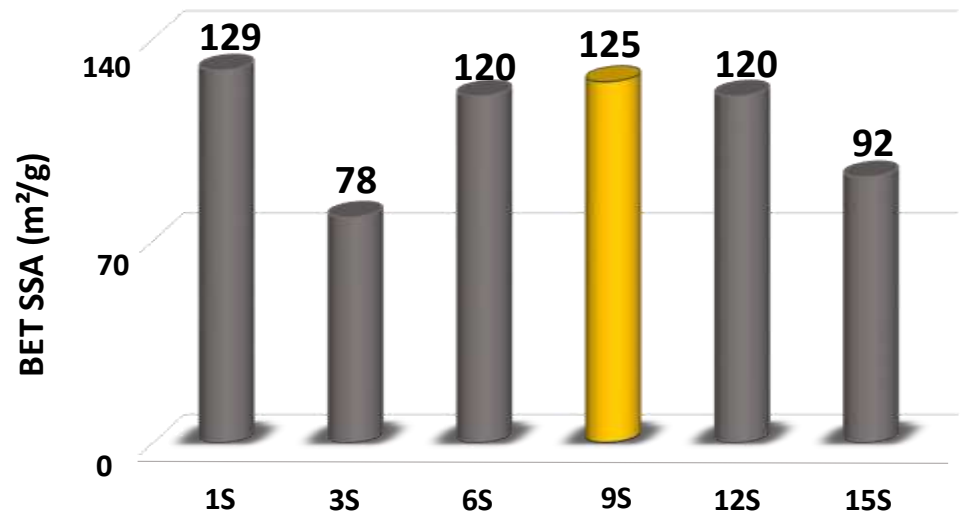

Figure 24. BET SSA values for $Ni_{0.6}Mn_{0.4}(OH)_2$ catalysts. Catalysts were prepared via chemical precipitation method using various NaOH(aq) concentrations. S stands for the stoichiometric NaOH concentration (i.e., 2.06 M).

Figure 24 suggests that $Ni_{0.6}Mn_{0.4}(OH)_2$-1S has the highest SSA value which is consistent with the broad XRD peaks observed in **Figure 22** for this material indicating poor structural order, high porosity, and a large number of structural imperfections/defects. It is apparent that a NaOH(aq) concentration of 1S is not sufficient for the establishment of an ordered α or β-metal hydroxide phases limiting the corresponding catalytic reactivity, despite a very high SSA of 129 m^2/g.

It can be realized that for higher NaOH(aq) concentrations than 1S, $Ni_{0.6}Mn_{0.4}(OH)_2$ catalysts show a volcano-type plot, where the SSA maximizes at 9S. Thus it can be argued that for NaOH(aq) > 1S, α/β mixed metal hydroxide domains can be constructed in an effective manner and increasing the base concentration up to 9S leads to the efficient hydroxylation of the metal hydroxide layers and possibly exfoliation of the 2D metal hydroxide layers resulting in increasing SSA. For excessive NaOH(aq) concentrations of > 9S, basic medium starts to damage the catalyst structure by increasing the relative abundance of β-domains as evident by the current XRD (**Figure 22**) and ATR-IR (**Figure 19b**) results. In addition, excessive hydroxylation of the catalyst surface at NaOH(aq) concentrations > 9S can also lead to the poisoning of the active metal cations on the surface by blocking these sites via -OH adsorption.

4.2.4. TEM and EDX Analysis

TEM images of the optimized $Ni_{0.6}Mn_{0.4}(OH)_2$-9S catalyst reveal a unique morphology (**Figure 25**). Two dimensional (2D) and layered structure of the $Ni_{0.6}Mn_{0.4}(OH)_2$-9S catalyst is evident in the TEM data in Figure 25, where $Ni_{0.6}Mn_{0.4}(OH)_2$-9S nanoparticles show a hexagonal/polyhedral geometry with an average diameter of 5-15 nm. Structural information deduced from TEM images are also consistent with the corresponding XRD data (**Figure 22**) suggesting the presence of a layered double hydroxide (LDH) crystal structure.

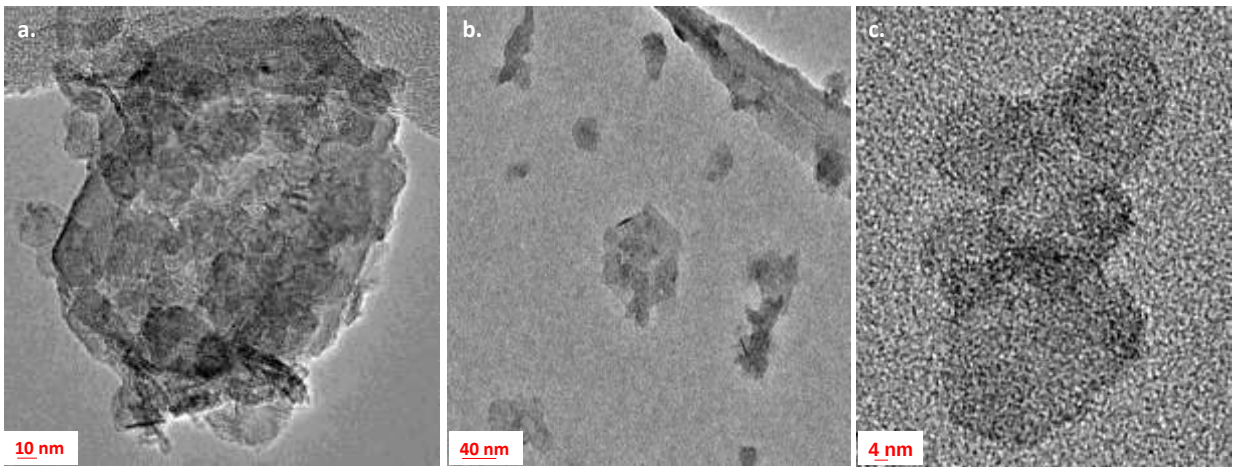

Figure 25. TEM images of the optimized $Ni_{0.6}Mn_{0.4}(OH)_2$-9S catalyst.

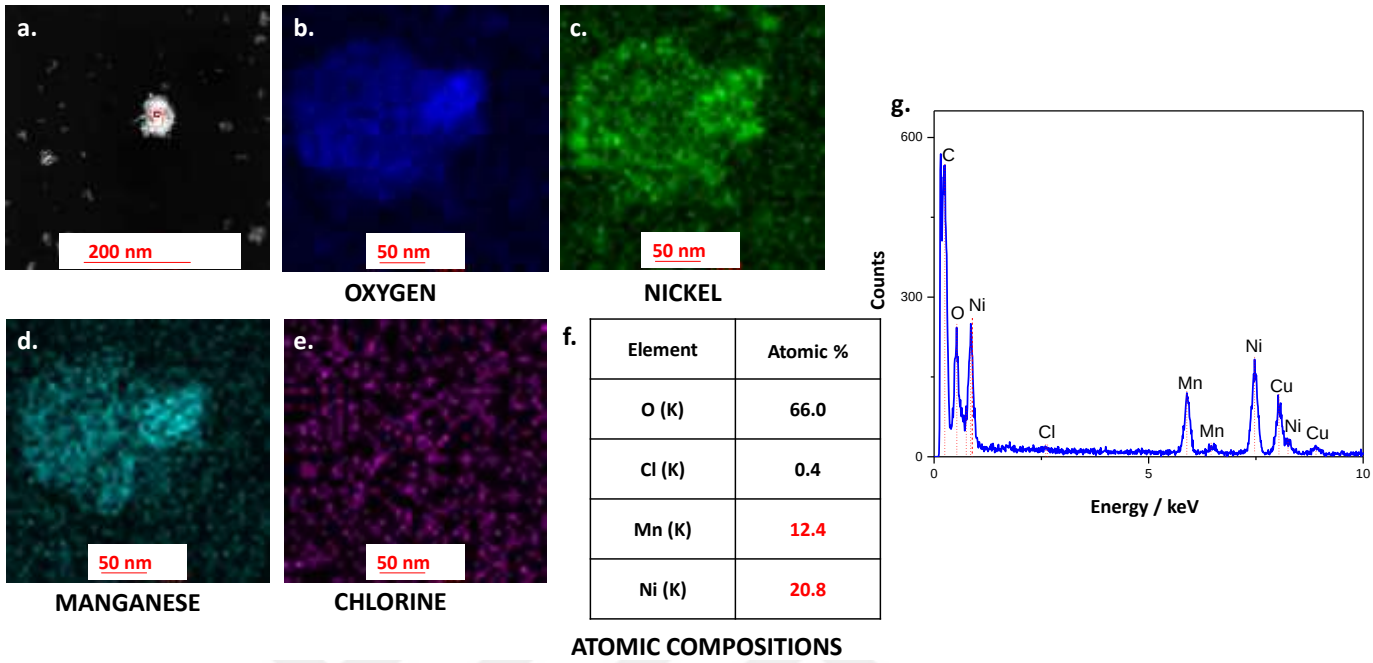

Figure 26. a.-e. TEM-EDX elemental mapping, f. EDX atomic percentages, g. EDX spectrum of the optimized $Ni_{0.6}Mn_{0.4}(OH)_2$-9S catalyst.

TEM/EDX analysis of the optimized $Ni_{0.6}Mn_{0.4}(OH)_2$ catalyst (**Figure 26**) verifies the co-presence of both Ni and Mn in the 2D catalyst particles where the atomic composition ratio of Ni:Mn was found to be 20.8:12.4, which corresponds to a stoichiometry of $Ni_{0.63}Mn_{0.37}(OH)_2$, in excellent agreement with the nominal metal precursor loading used in the synthesis. EDX data also clearly indicates that the chloride ions of the metal precursors are entirely replaced with hydroxide functionalities during the synthesis which was carried out under basic conditions (i.e., NaOH(aq) of 9S = 18.54 M).

4.2.5. Surface Chemical and Electronic Structural Analysis via XPS Measurements

Surface atomic compositions of the synthesized mixed metal hydroxide samples were investigated via XPS (**Figures 27** and **28**). **Figure 27** illustrates that surface concentration of Ni atoms monotonically increase with the increasing nominal Ni precursor concentration used in the synthesis. Furthermore, **Figure 28** shows that varying NaOH(aq) concentrations used in the synthesis does not yield a clear trend in the surface atomic composition of the elements present on

the catalysts. However, the data given in **Figure 28** clearly points out to the fact that a NaOH(aq) concentration of 1S is not sufficient to remove all of the chloride ions coming from the metal precursors and the complete chloride removal is observed for NaOH(aq) concentrations ≥ 9S. It can also be argued that chloride ions detected in some of these mixed metal hydroxides enable charge compensation (i.e., electrical neutrality) of the overall ionic structure. As will be shown in the analysis of the Mn3s XPS data, oxidation of a Mn^{2+} sites to mostly Mn^{3+} species and with a lesser extent to and Mn^{4+} species during the synthesis necessitates the presence of additional anions in the structure to compensate for the increasing cationic charge.

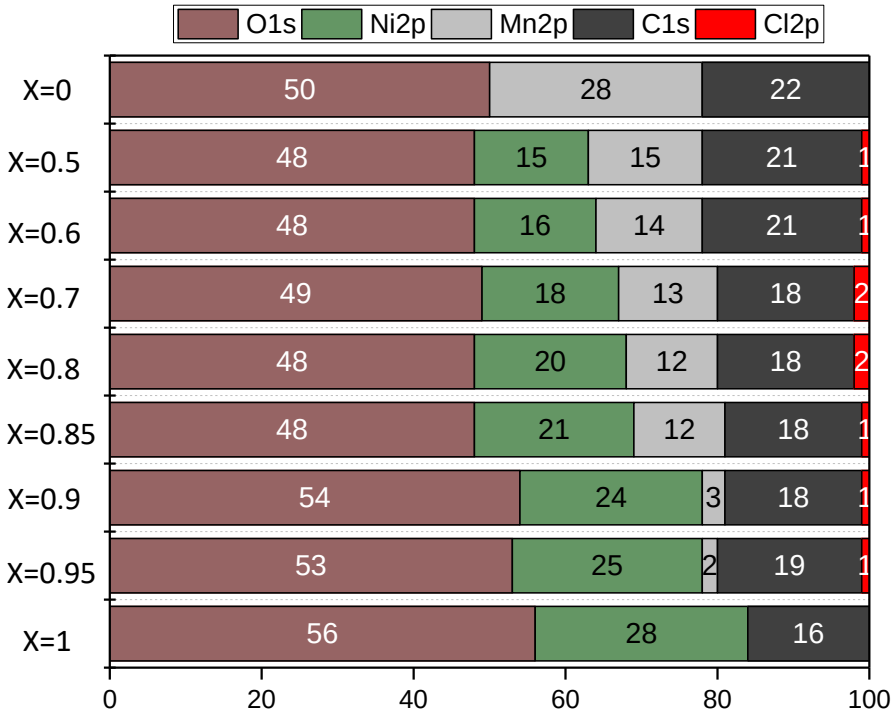

Figure 27. XPS surface atomic composition values for $Ni_xMn_{1-x}(OH)_2$ catalysts. Catalysts were prepared via chemical precipitation method using various Ni and Mn precursor amounts and a NaOH(aq) concentration of 6S. S stands for the stoichiometric NaOH concentration (i.e., 2.06 M).

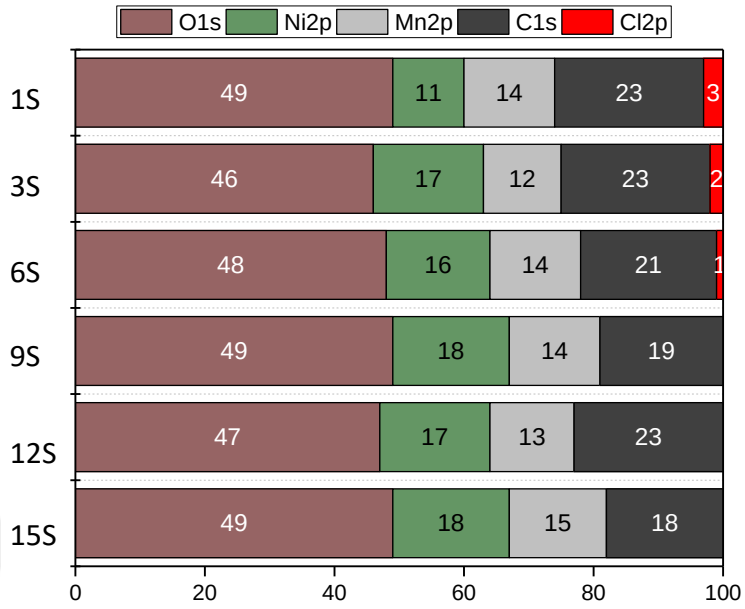

Figure 28. XPS surface atomic composition values for $Ni_{0.6}Mn_{0.4}(OH)_2$ catalysts. Catalysts were prepared via chemical precipitation method using various NaOH(aq) concentrations. S stands for the stoichiometric NaOH concentration (i.e., 2.06 M).

To further understand how Mn changes its oxidation state for $Ni_{0.6}Mn_{0.4}(OH)_2$ synthesized from various NaOH concentrations, a vital XPS feature that had to be considered was the peak splitting in the Mn 3s spectra. The Mn 3s core level peak splitting arises from the exchange coupling between the 3s hole and the 3d electrons. The magnitude of this peak splitting is proportional to (2X+1), where X is the local spin of the 3d electrons in the ground state. [80] Kisinger et. al. explained that the 3s peak splitting arises from the multiple final states in the core level XPS of 3d transition metal compounds during the screening process. During this process, the ejection of a core electron leads to a number of final states. In 3d transition metal compounds, two major final states exist after the ejection of a core electron. One in which the electronic state of the ground state is preserved and the other in which an electron is transferred from the ligand onto the transition metal ion. In Mn, when valence d^n configuration and the ligand configuration L hybridize to form a bonding and an antibonding orbital, d^nL configuration is the lowest one while $d^{n+1}L^{-1}$ configuration is the highest one in the final state. These final state configurations exhibit a net spin and when this spin interact with the spin of the core hole, peak split in 3s spectrum is observed.[108]

Although the Mn 2p signal is the most intense peak for Mn, due to its convoluted nature, it is not very sensitive to the changes in oxidation state of the surface Mn species.

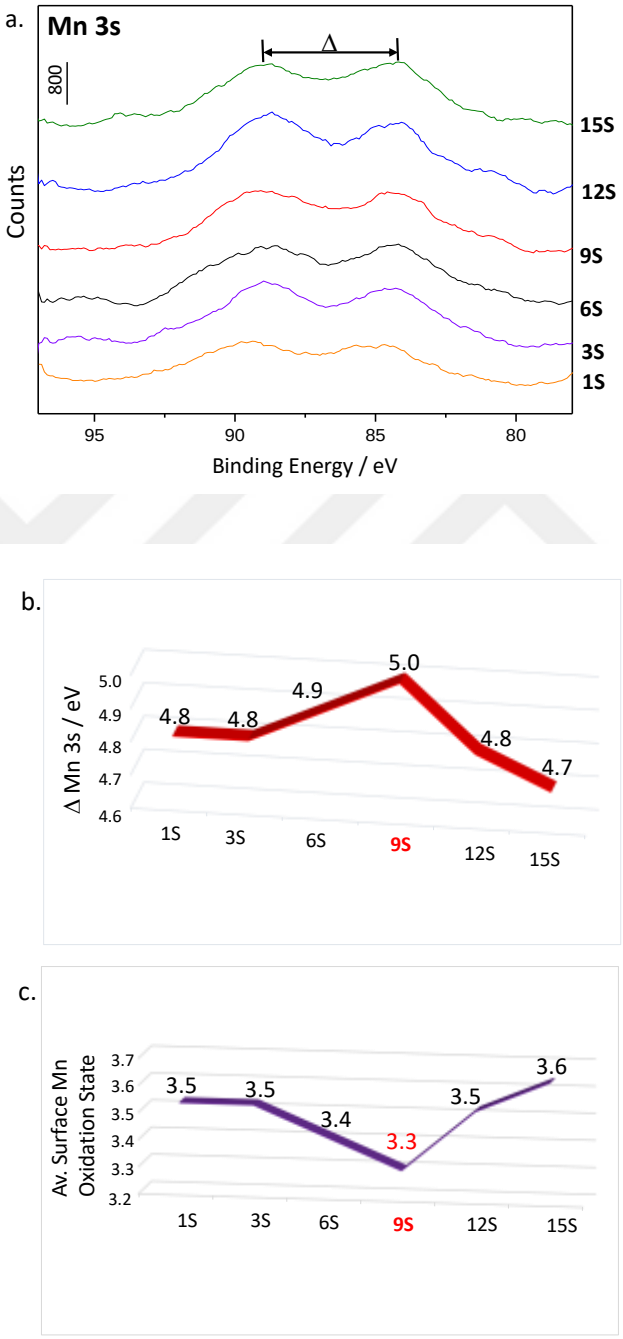

Figure 28. a) Mn 3s spectra, b) Binding energy splitting values of the Mn 3s signals (Δ Mn 3s), c) Average oxidation state of surface Mn species for $Ni_{0.6}Mn_{0.4}(OH)_2$ synthesized with different NaOH(aq) concentrations. S stands for the stoichiometric NaOH concentration (i.e., 2.06 M)

However, peak splitting values of Mn 3s can give useful information on the changes in oxidation state of the surface Mn species. This peak splitting value when inserted into the equation, AOS = 8.95-1.13Δ, [47] can allow estimation of the average oxidation state of the surface manganese species.

In light of the XPS analysis, $Ni_{0.6}Mn_{0.4}(OH)_2$-9S i.e., the ultimately optimized catalyst, exhibited the smallest surface Mn average oxidation state of +3.3 (**Figure 28c**). Hence, in addition to the other structural factors described above, unique surface Mn oxidation sate in $Ni_{0.6}Mn_{0.4}(OH)_2$-9S seems to be closely related to its superior catalytic activity in aerobic oxidation of xanthene to xanthone.

4.2.6. Thermal Stability Analysis via TGA Measurements

TGA analysis can be quite informative to avoid catalyst destruction during the regeneration and pretreatment protocols which can be designed to elongate catalyst life-time. Weight loss events observed in the TGA experiment presented in **Figure 29** can be divided into four stages. In the first stage, a weight loss of 5.2% was detected at 102 °C. The second stage led to a 11.4% weight loss, at 230 °C. The third and fourth stages corresponded 1.7% and 2.1% weight losses at 413 °C and 624 °C, respectively. These four different stages of weight loss can be explained using the former literature studies. [12] The first stage can be attributed to the removal of chemisorbed water from the surface. In the second stage, most of interlayered bulk water desorbed from the material. During the third stage, dehydroxylation process began and at the end of the fourth stage, the metal hydroxide phase was completely dehydroxylated and converted destroyed to oxide phase(s).

With this in mind, we decided to choose 300 °C (i.e. end of the second weight loss stage in the TGA data) as the regeneration and pretreatment temperature in an attempt to preserve the structural integrity of the material, while thermally removing unwanted species from the catalyst surface for the rejuvenation of the material.

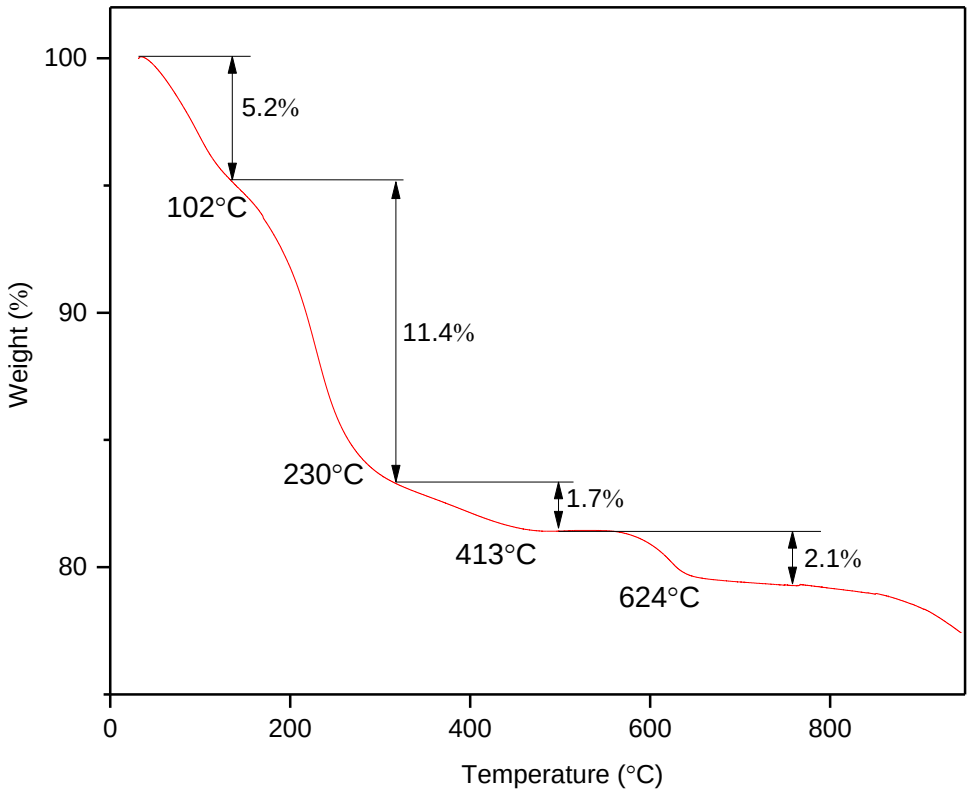

Figure 29. TGA analysis of $Ni_{0.6}Mn_{0.4}(OH)_2$-9S catalyst.

4.3. Catalyst Re-usability and Regeneration Studies

In an attempt to test the stability of the ultimately optimized catalyst in alkylarene oxidation reactions, reusability experiments were conducted. In the reusability experiments, we preferred to use fluorene as the substrate rather than xanthene. This was because while the fluorene experiments required 20 mg of the optimized $Ni_{0.6}Mn_{0.4}(OH)_2$-9S catalyst, xanthene experiments needed only 7 mg of the optimized catalyst. Hence, due to the larger experimental errors associated with the accurate recovery of the small amount (7 mg) of catalyst in xanthene experiments, we decided to use fluorene as the substrate.

During the reusability studies (without regeneration), >99% fluorene conversion was obtained in the first cycle. The second and third cycles yielded 61% and 19% fluorene conversion, respectively (**Figure 30a**). Decrease in the conversion in the subsequent cycles led us to carry out a regeneration protocol to regain the performance. Having the currently performed TGA analysis in mind, we

decided to come up with a regeneration protocol that could help with the restoration of the spent catalyst.

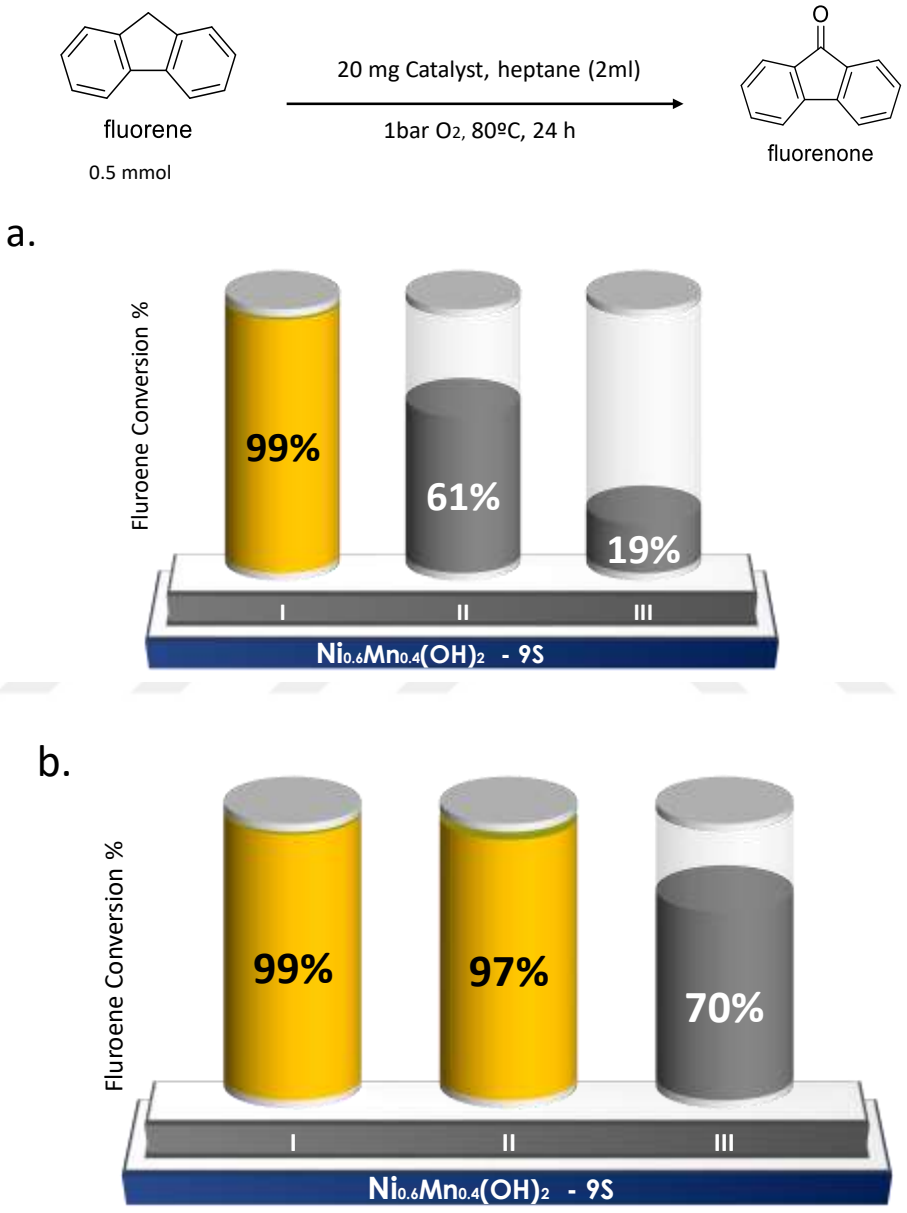

Figure 30. Catalytic activity data for optimized $Ni_{0.6}Mn_{0.4}(OH)_2$-9S catalyst in the aerobic oxidation of fluorene to fluorenone: a) without regeneration, b) with regeneration. "I" represents the 1st cycle activity, "II" represents the 2nd cycle activity, and "III" represent s the 3rd cycle activity.

The regeneration protocol was comprised of annealing the spent catalyst at 300 °C for 6 h (before the 2nd cycle), and 12 h (before the 3rd cyle) under 100 sccm 99.999% Ar(g) flow in a flow furnace.

With this regeneration protocol, the catalyst recovered its initial activity almost completely in the second cycle and performed very well in the third cycle with a relatively moderate loss in activity (**Figure 30b**).

In other to understand the effect of the regeneration protocol on the spent catalyst, ATR-IR spectroscopic studies were conducted on the fresh, spent and regenerated optimized $Ni_{0.6}Mn_{0.4}(OH)_2$-9S catalyst, with the aim of investigating the functional group changes occurring on these surfaces (**Figure 31**).

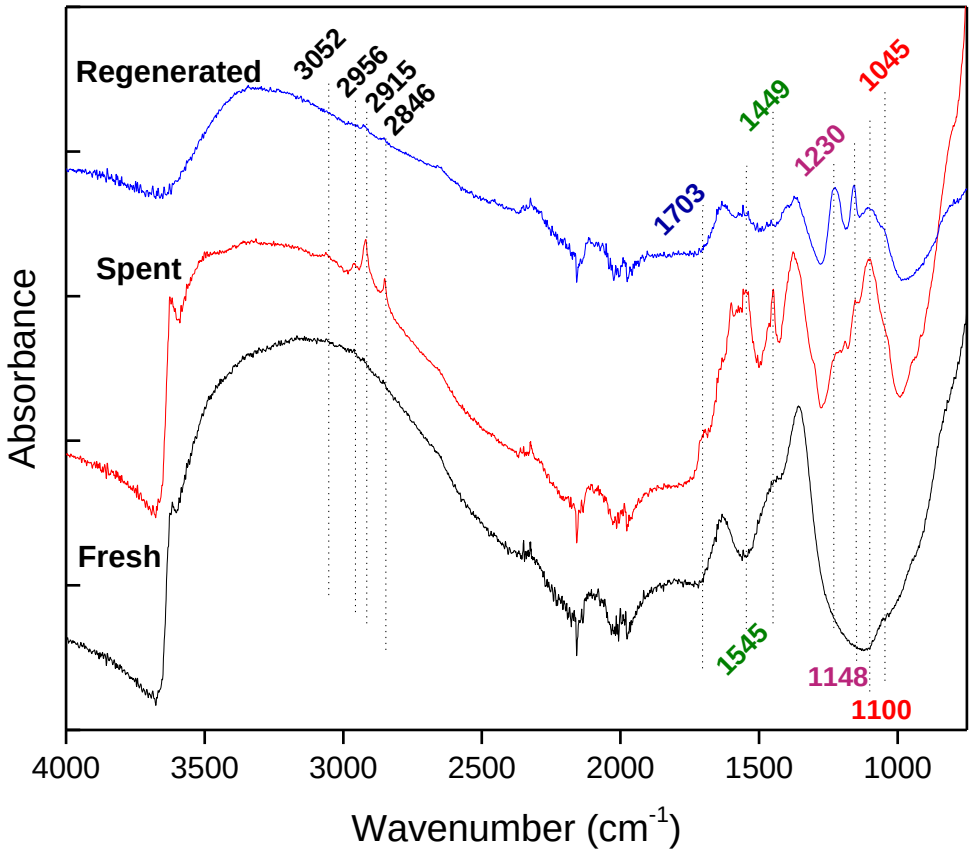

Figure 31. ATR-FTIR spectra of the fresh, spent and regenerated optimized $Ni_{0.6}Mn_{0.4}(OH)_2$-9S catalysts.

Assignment of the vibrational features in the ATR-IR spectra given in **Figure 31** is achieved by using the conventional infrared signatures of common organic functional groups. [81-82] Spectral features at 1045 cm^{-1} and 1100 cm^{-1} can be assigned to -C(sp^3)-O stretching, while the IR signals at 1148 cm^{-1} and 1230 cm^{-1} can be attributed to -C(sp^2)-O stretching. Carbonate features were

recorded at 1449 cm^{-1} and 1545 cm^{-1}. On the other hand, the feature seen at 1703 cm^{-1} can be assigned to -CH or -CH_2 bending modes. Spectral features within 2845 - 3053 cm^{-1} can be attributed to aliphatic -CH_x stretchings. **Figure 31** suggests that after the utilization of the catalyst, various organic residues are deposited on the spent catalyst surface, blocking and poisoning the catalytic active sites. On the other hand, most of these poisoning species can be eliminated after the regeneration protocol.

4.4. Mechanistic Studies on Xanthene Oxidation

In order to investigate the time-dependent conversion of xanthene to xanthone using the optimized $Ni_{0.6}Mn_{0.4}(OH)_2$-9S catalyst, we performed additional experiments shown in **Figure 32**. Time-dependent xanthene conversion presented in **Figure 32** illustrates after 6 h, 82 % of xanthene was converted into xanthone, without the formation of any other side products. The 12^{th}, 18^{th} and 24^{th} hours recorded conversions of 96%, 97% and >99%, respectively. These time-dependent experiments indicate that the catalytic aerobic oxidation of xanthene to xanthone is practically completed after 12 h.

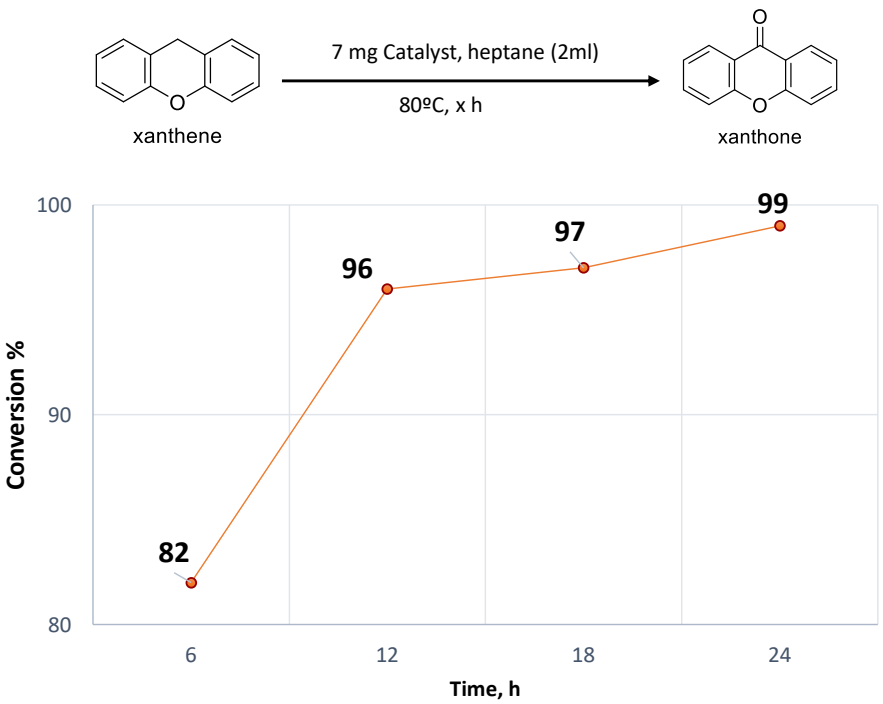

Figure 32. Time-dependent conversion of xanthene to xanthone using the optimized $Ni_{0.6}Mn_{0.4}(OH)_2$-9S catalyst.

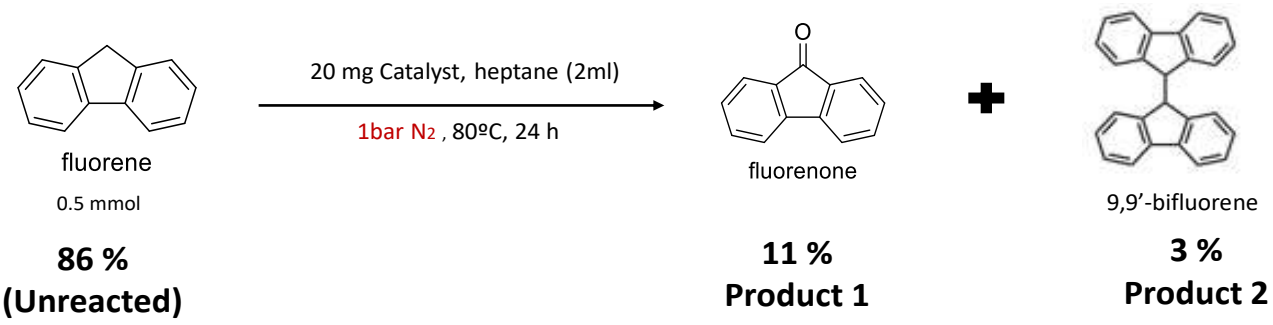

Figure 33. Freeze-pump-thaw experiment to probe the effect of O_2 on the catalytic aerobic oxidation of fluorene to fluorenone outcome. Catalyst used in this experiment was the optimized $Ni_{0.6}Mn_{0.4}(OH)_2$.

Along these lines, experiments were carried out in the absence of gaseous molecular oxygen in the reaction medium. This is achieved by conducting freeze-pump-thaw series before the reaction in

order to deoxygenate the reaction mixture. This is followed by the execution of the catalytic activity tests in the absence of molecular gaseous oxygen by filling the reactor with 1 bar N_2(g) (purity > 99.9%). In these control experiments utilizing the optimized $Ni_{0.6}Mn_{0.4}(OH)_2$-9S catalyst, fluorene and n-heptane were used as the substrate and the solvent, respectively. When the reaction mixture and the optimized catalyst was heated in the absence of O_2(g) at 80 °C for 24 h, two major products were detected. Fluorenone product was observed to form with 11% conversion and 9,9'-bifluorene product was formed with 3% conversion. The rest of the post reaction medium contained 86% of the unreacted fluorene (**Figure 32**). These results suggest that while a small amount of fluorenone (i.e., the major oxidation product in the presence of O_2(g)) can also be formed under anaerobic conditions, its formation (and thus C-H activation) requires the utilization of O_2(g). Furthermore, in the absence of O_2(g), minor side reactions can also occur, yielding 9,9'-bifluorene side product which was absent in the aerobic catalytic oxidation of fluorene.

4.5. Heterogeneous Catalytic Low-Temperature Carbon Monoxide (CO) Oxidation using Mixed Metal Hydroxides

In order to demonstrate the utility of the mixed metal hydroxide catalytic systems in gas phase catalysis, low-temperature CO oxidation catalytic activity tests were carried out. **Figures 33** and **34** present the CO oxidation activities of the optimized $Ni_{0.6}Mn_{0.4}(OH)_2$-9S catalyst along with a conventional PGM-based benchmark catalyst (i.e., 1 wt. % Pt/Al_2O_3) at room temperature and upon linear heating to various temperatures, respectively. At room temperature, the pretreated optimized $Ni_{0.6}Mn_{0.4}(OH)_2$-9S catalyst showed promising activity within the duration of the room temperature experiment (i.e., 6 h). This catalyst showed an initial room temperature CO conversion of 70% which dropped to about 10% at the 6th hour. This was probably due to CO poisoning of the active sites. On the other hand, the pretreated commercial benchmark catalyst, 1 wt. % Pt/Al_2O_3, was not active at all at room temperature.

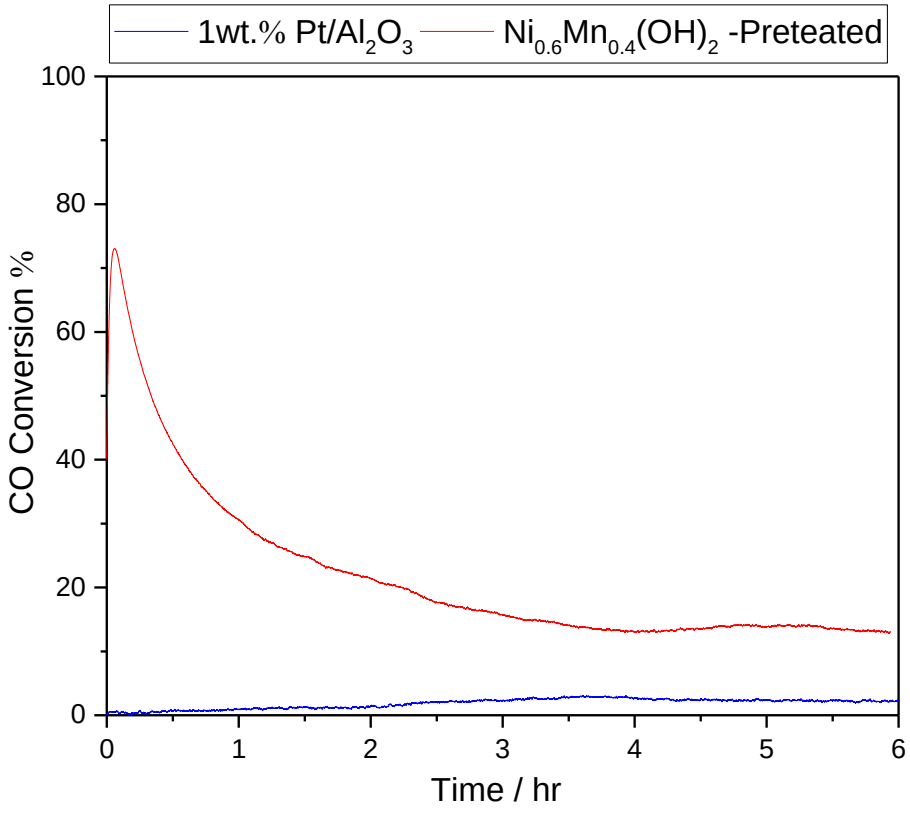

Figure 34. Room temperature catalytic CO oxidation test on pre-treated $Ni_{0.6}Mn_{0.4}(OH)_2$-9S and pretreated commercial 1 wt. % Pt/Al_2O_3 PGM benchmark catalysts. (Gas feed: 1% CO + 20% O_2 where Ar was used as the balance gas).

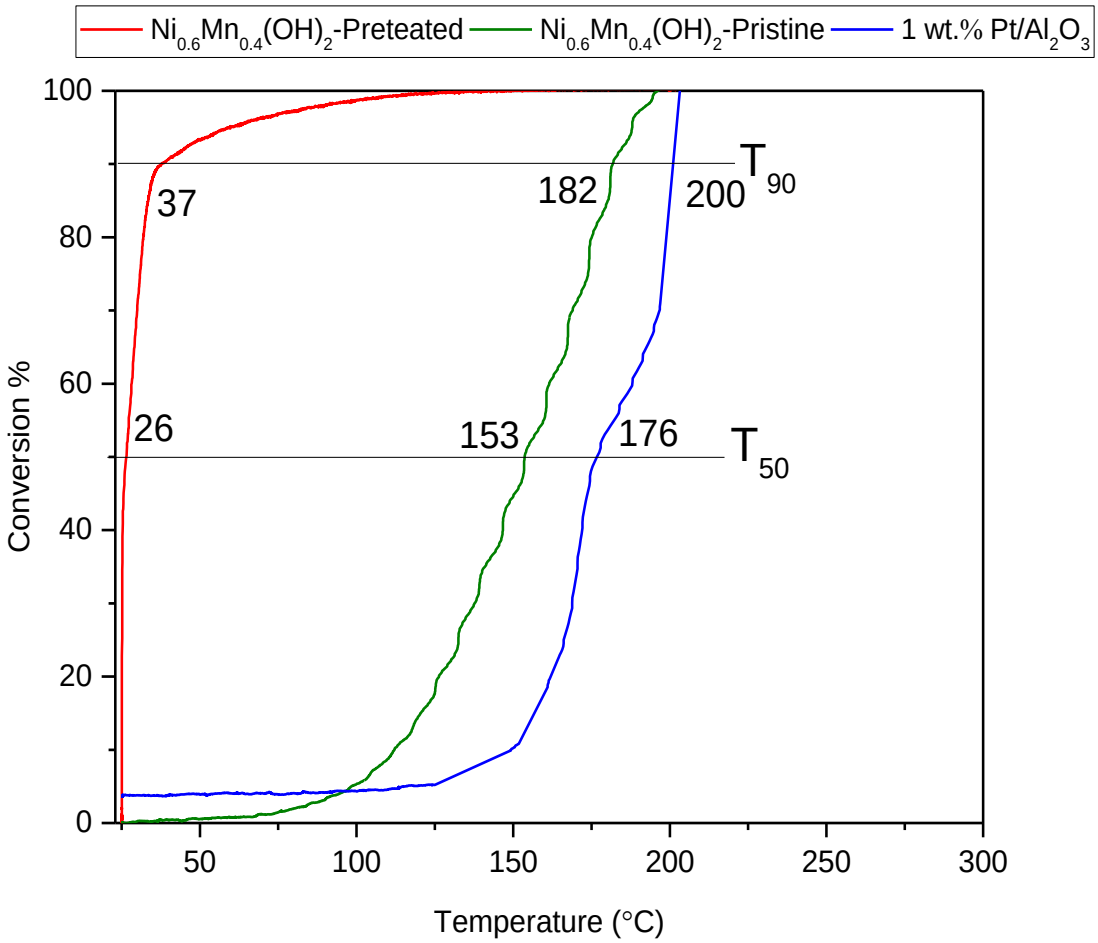

Figure 35. Variable temperature catalytic CO oxidation test on pristine $Ni_{0.6}Mn_{0.4}(OH)_2$-9S, pre-treated $Ni_{0.6}Mn_{0.4}(OH)_2$-9S, and pretreated commercial 1 wt. % Pt/Al_2O_3 PGM benchmark catalysts. (Gas feed: 1% CO + 20% O_2 where Ar was used as the balance gas).

In catalytic CO oxidation tests, T_{50} which is the temperature at 50% CO conversion is defined to be the light-off temperature, while T_{90} is the temperature where there is 90% CO conversion to CO_2. It can be seen in **Figure 35** that the pristine $Ni_{0.6}Mn_{0.4}(OH)_2$-9S catalyst showed better catalytic CO oxidation performance than that of the 1 wt. % Pt/Al_2O_3 PGM benchmark catalyst in terms of both T_{50} and T_{90}. While the pristine $Ni_{0.6}Mn_{0.4}(OH)_2$-9S catalyst yielded T_{50} and T_{90} values of 153 ^oC and 182 ^oC, respectively, the PGM benchmark catalyst revealed T_{50} and T_{90} values of 176 ^oC and 200 ^oC, respectively. Pristine $Ni_{0.6}Mn_{0.4}(OH)_2$-9S catalyst performed even better after it underwent a pretreatment protocol (which included annealing of the pristine $Ni_{0.6}Mn_{0.4}(OH)_2$-9S catalyst at 300 °C in 500 sccm 99.9% Ar(g) flow for 1 h in the catalytic bed before the CO oxidation

reaction). The T_{50} and T_{90} values for the pretreated $Ni_{0.6}Mn_{0.4}(OH)_2$-9S catalyst were 26 °C and 32 °C, respectively.

CHAPTER 5

5. Conclusion

In this work, we synthesized novel catalytic mixed metal hydroxides exhibiting unique 2D structure, morphology, crystallographic and electronic properties. Characterization and spectroscopic studies revealed that the optimized catalyst was in the form of $Ni_{0.6}Mn_{0.4}(OH)_2$, synthesized from 9S, where S is 2.06M stoichiometric NaOH(aq) concentration. Furthermore, a novel regeneration protocol was also developed to fully retain the initial activity of the catalyst after its use in the xanthene oxidation reaction. Compared to the existing catalysts in the literature results, $Ni_{0.6}Mn_{0.4}(OH)_2$-9S catalyst revealed the best catalytic performance per gram of catalyst in the catalytic aerobic oxidation of xanthene to xanthone. In addition to the superior catalytic activity of the $Ni_{0.6}Mn_{0.4}(OH)_2$-9S catalyst in liquid phase organic partial oxidations, its activity in gas phase oxidation reactions was also demonstrated using low-temperature CO oxidation reaction. $Ni_{0.6}Mn_{0.4}(OH)_2$-9S catalyst was found to outperform conventional PGM-based benchmark catalyst in low-temperature CO oxidation. Current results clearly demonstrate that chemically fine-tuned mixed metal hydroxide systems can provide promising catalytic alternatives in low temperature liquid phase organic reactions as well as gas phase oxidation reactions.

References

[1] A. Beniya, S. Higashi, *Nat Catal* **2019**, 2, 590–602.

[2] S. Royer, D. Duprez, F. Can, X. Courtois, C. Batiot-Dupeyrat, S. Laassiri, H. Alamdari, *Chem. Rev.* **2014**, 114, 20, 10292–10368.

[3] Y. Xin, Q. Li, Z. Zhang, *ChemCatChem* **2017**, 10(1), 29–41.

[4] K. Yamaguchi, N. Mizuno, *Angew. Chem.* **2002**, 114, 4720-4724.

[5] I.S. Nielsen, E.Taarning, K. Egeblad, et al. *Catal Lett* **2007**, 116, 35–40.

[6] A.B. Powell, S.S. Stahl, *Org. Lett.* **2013**, 15, 19, 5072–50757.

[7] N. Kumar, K. Naveen, A. Bhatia, S. Muthaiah, V. Siruguri, A.K. Paul, *React. Chem. Eng.*, **2020**, 5, 1264.

[8] B.-Z. Zhang, M.A. White, T.-K. Sham, J.A. Pincock, R.J. Doucet, K.V.R. Rao, K.N. Robertson, T.S. Cameron, *J. Am. Chem. Soc.* **2003**, 125, 8, 2195–2199.

[9] Z. Yan, X. Yu, Y. Zhang, H. Jia, Z. Sun, P. Du, *Appl. Catal. B*, **2014**, 160–161, 173–178.

[10] J. Ran, J. Yu, M. Jaroniec, *Green Chem.*, **2011**, 13, 2708–2713.

[11] M. Gao, W. Sheng, Z. Zhuang, Q. Fang, S. Gu, J. Jiang, Y. Yan, *J. Am. Chem. Soc.*, **2014**, 136, 7077–7084.

[12] D.S. Hall, D.J. Lockwood, C. Bock, B.R. MacDougall. *Proc. R. Soc. A*, **2015**, 471: 20140792.

[13] H. Bode, K. Dehmelt, J. Witte, *Electrochim. Acta*, **1966**, 11, 1079–1087.

[14] K. Gholivand, M. Hosseini, A.A.E. Valmoozi, K. Farshadfar, *CrystEngComm*, **2017**, 19, 2536.

[15] A. Livingstone, D. Bish, *Mineral. Mag.* **1982**, 46, 1–5.

[16] RS. McEwen, *J. Phys. Chem.* **1971**, 75, 1782–1789.

[17] R. Barnard, C.F. Randell, F.L. Tye. Studies concerning the ageing of α and β-$Ni(OH)_2$ in relation to nickel–cadmium cells. In *Proc. 12th Int. Power Sources Symp. Brighton, September 1980* (ed. J Thompson), **1981**, pp. 401–425. London, UK Academic Press.

[18] S. Le Bihan, J. Guenot, M. Figlarz, *C. R. de l'Académie des Science: Paris,* **1970**, 270, 2131–2133.

[19] M. Rajamathi, P.V. Kamath. *J. Power Sources,* **1998**, 70, 118–121.

[20] J. McBreen, Nickel hydroxides. In *Handbook of battery materials* (eds C Daniel, JO Besenhard), **2011**, pp. 149–168, 2nd edn.Weinheim, Germany:Wiley-VCH Verlag GmbH & Co. KGaA.

[21] W. Dennstedt, W. Löser, *Electrochim. Acta*, **1971**, 16, 429–435.

[22] A. Audemer, A. Delahaye, R. Farhi, N. Sac-Epée, J-M. Tarascon, *J. Electrochem. Soc.* **1997**, 144, 2614–2620.

[23] M.B.J.G. Freitas, *J. Power Sources,* **2001**, 93, 163–173.

[24] B. Mani, J.P. de Neufville, *J. Electrochem. Soc.* **1988**, 135, 800–803.

[25] F.P. Kober, *J. Electrochem. Soc.* **1967**, 114, 215–218.

[26] C. Greaves, M.A. Thomas, *Acta Crystallogr. Sect. B: Struct. Sci.,* **1986**, 42, 51–55.

[27] P. Jeevanandam, Y. Koltypin, A. Gedanken, *Nano Lett.,* **2001**, 1, 263–266.

[28] F.P. Kober, On the structure of electrochemically active hydrated nickel-oxide electrodes.mIn *Power Sources: Proceedings for the 5th International Power Sources Symposium* (ed. DHCollins), **1967**, pp. 257–268. Brighton, London: Academic Press.

[29] A.V. Radha, P.V. Kamath, C. Shivakumara, *Acta Crystallogr. Section B,* **2007**, 63, 243–250.

[30] T.N. Ramesh, *Mater. Chem. Phys.,* **2009**, 114, 618–623.

[31] C. Tessier, P.H. Haumesser, P. Bernard, C. Delmas, *J. Electrochem. Soc.*, **1999**, 146, 2059–2067.

[32] L. Guerlou-Demourgues, C. Denage, C. Delmas, *J. Power Sources*, **1994**, 52,269–274.

[33] F. Zhou, X. Zhao, A. van Bommel, A.W. Rowe, J.R. Dahn, *Chem. Mater.*, **2009**, 22, 1015–1021.

[34] C. Delmas, C. Faure, Y. Borthomieu, *Mater. Sci. Eng.: B*, **1992**, 13, 89–96.

[35] M. Rajamathi, P. Vishnu Kamath, R. Seshadri, *J. Mater. Chem.*, **2000**, 10, 503–506.

[36] M.N. Rajamathi, G. Subbanna, P.Vishnu Kamath, *J. Mater. Chem.*, **1997**, 7, 2293–2296.

[37] T.N. Ramesh, R.S. Jayashree, P.V. Kamath, *Clays Clay Miner.*, **2003**, 51, 570–576.

[38] A.P. Hauel, *Trans. Electrochem. Soc.*, **1939**, 76, 435–452.

[39] J-C. Chen, C-T. Hsu, C-C. Hu, *J. Power Sources*, **2014**, 253, 205–213.

[40] J. Huang, T. Lei, X. Wei, X. Liu, T. Liu, D. Cao, J. Yin, G. Wang, *J. Power Sources*, **2013**, 232, 370–375.

[41] R. Mortimer, M. Sialvi, T. Varley, G. Wilcox, *J. Solid State Electrochem.*, **2014**, 18, 3359–3367.

[42] Y. Fan, Z. Yang, X. Cao, P. Liu, S. Chen, Z. Cao, *J. Electrochem. Soc.*, **2014**, 161, B201–B206.

[43] H. Zou, F. Guo, M. Luo, Q. Yao, Z-H. Lu, *Int. Journal of Hydrogen Energy*, **2020**, 11641-11650.

[44] P. Gandeepan, T. Müller; D. Zell, G. Cera, S. Warratz, L. Ackermann, *Chem. Rev*. **2019**, *119*, 2192-2452.

[45] Z. Guo, B. Liu, Q. Zhang, W. Deng, Y. Wang, Y. Yang, *Chem. Soc. Rev*., **2014**, *43*, 3480-3524.

[46] For a review on C-H functionalization reactions of diarylmethanes, see: U. Gulati, R. Gandhi, J. K. Laha, Benzylic Methylene Functionalizations of Diarylmethanes. *Chem. Asian J.* **2020**, *15*, 3135-3161.

[47] S. Nakai, T. Uematsu, Y. Ogasawara, K. Suzuki, K. Yamaguchi, N. Mizuno, *ChemCatChem* **2018**, 10, 1096 – 1106.

[48] S. Shibata, K. Sugahara, K. Kamata, M. Hara, *Chem. Commun.*, **2018**, 54, 6772—6775.

[49] K. Sugahara, K. Kamata, S. Muratsugu, M. Hara, *ACS Omega* **2017**, 2, 1608−1616.

[50] S. Kawasaki, K. Kamata, M. Hara, *ChemCatChem* **2016**, 8, 3247 – 3253.

[51] Y. Sahin, A.T. Sika-Nartey, K.E. Ercan, Y. Kocak, S. Senol, E. Ozensoy, Y.E. Türkmen, *ACS Appl Mater Interfaces.* **2021** , doi: 10.1021/acsami.0c20490.

[52] A.Shaabani, S. Shaabani and H. Afaridoun, *RSC Adv.*, **2016**, 6, 48396–48404.

[53] A. Yoshida, Y. Takahashi, T. Ikeda, K. Azemoto, S. Naito, *Catalysis Today*, **2011**, 164, 332–335.

[54] H. Kawabata, M. Hayashi, *Tetrahedron Letters*, **2004**, 45 5457–5459.

[55] B. Chen, F. Li, Z. Huang, T. Lu, Y.Yuan, J. Yu, G. Yuan et. al. *RSC Adv.*, **2012**, 2, 11449–11456.

[56] A. Shaabani, Z. Hezarkhani, M.K. Nejad, *J Mater Sci*., **2017**, 52, 96–112.

[57] B. Majumdar, T.Bhattacharya, T. K. Sarma, *ChemCatChem* **2016**, 8, 1825 – 1835.

[58] A. Shaabani, S. Keshipour, M. Hamidzad, S. Shaabani, *Journal of Molecular Catalysis A: Chemical*, **2014**, 395, 494–499.

[59] C. Hong, J. Ma, M. Li, L. Jin, X. Hu, W. Mo, B. Hu, N. Sun, Z. Shen, *Tetrahedron* **2017**, 73, 3002-3009.

[60] K. Kamata, J. Kasai, K. Yamaguchi, N. Mizuno, *Org. Lett.* **2004**, 6, 20, 3577–3580.

[61] A. Shaabani, M.B. Boroujeni, M.H. Sangachin, *J. Chem. Sci.* **2015**, 127, 11, 1927–1935.

[62] A. Shaabani, Z. Hezarkhani, E. Badali, *RSC Adv*., **2015**, 5, 61759.

[63] A. Shaabani, Z. Hezarkhani, S. Shaabani, *RSC Adv.*, **2014**, 4, 64419–64428.

[64] S.-I. Fujita, K. Yamada, A. Katagiri, H. Watanabe, H. Yoshida, M. Arai, *Applied Catalysis A: General*, **2014**, 488, 171–175.

[65] A. Shaabani, M.B. Boroujeni, M.S. Laeini, *Appl. Organometal. Chem.* **2016**, 30, 154–159.

[66] T. Uematsu , Y. Miyamoto , Y. Ogasawara , K. Suzuki , K. Yamaguchi, N. Mizuno, *Catal. Sci. Technol.*, **2016**, 6, 222–233.

[67] X. Xie, Y. Li, ZQ. Liu et al, *Nature*, **2009**, 458, 746–749.

[68] Q. Huang, X. Yan, B. Li, X. Xu, Y. Chen, S. Zhu, S. Shen, *Journal of Industrial and Engineering Chemistry*, 2013, 19, 2, 438-443.

[69] M. Zammit, C. DiMaggio, C. Kim, C. Lambert, G. Muntean, C. Peden, J. Parks, K. Howden, *Future Automotive Aftertreatment Solutions: The 150 °C Challenge Workshop Report*. Available online: https://cleers.org/low-temperature-protocols/ (accessed on 05.01.2021).

[70] D.L. Trimm, & Z.I. Onsan, Catal. Rev. Sci. Eng., 2001, 43, 31–84.

[71] S.H. Oh, & G.B. Hoflund, *J. Catal*., **2007**, 245, 35–44.

[72] S. Royer, D. Duprez, *ChemCatChem*, 2011, 3, 24−65.

[73] Y. B. Yu, T. Takei, H. Ohashi, H. He, X. L. Zhang, M. Haruta, *J. Catal*. **2009**, 267, 121−128.

[74] F. Zhou, X. Xhao, A. van Bommel, A.W. Rowe, J.R. Dahn, *Chemistry of Materials*, **2010**, 22, 1015–1021.

[75] Y.-R. Luo, Handbook of Bond Dissociation Energies in Organic Compounds, CRC Press, Boca Raton, **2003**.

[76] K. Rakus, S. P. Verevkin, J. Schätzer, H.-D. Beckhaus, C. Rüchardt, *Chem. Ber.* **1994**, *127*, 1095-1103.

[77] C. Rüchardt, M. Gerst, J. Ebenhoch, *Angew. Chem. Int. Ed.* **1997**, *36*, 1406-1430.

[78] V. D. Parker, K. L. Handoo, F. Roness, M. Tilset, *J. Am. Chem. Soc.* **1991**, *113*, 7493-7498.

[79] S.D. Hall, D.J. Lockwood, S. Poirier, C. Bock, B.R. MacDougall, *J. Phys. Chem. A*, **2012**, 116, 6771−6784.

[80] V. R. Galakhov, M. Demeter, S. Bartkowski, M. Neumann, N. A. Ovechkina, E. Z. Kurmaev, N. I. Lobachevskaya, Ya. M. Mukovskii, J. Mitchell, D. L. Ederer, *Physical Review B*, **2002**, 65, 113102.

[81] B. Klingenberg, M. A. Vannice, Chem. Mater., 1996, 8, 12, 2755–2768

[82] T. Levan, M. Che, J.M. Tatibouet, M. Kermarec,, Journal of Catalysis, 1993, 142, 18-26.

[83] L. Guerlou-Demourgues, C. Delmas, *J. Electrochem. Soc.* **1996**, 143, 561–566.

[84] X. Chen, C. Long, C. Lin, T. Wei, J. Yan, L. Jiang, Z. Fan *Electrochim. Acta* **2014**, 137, 352–358.

[85] R.S. Jayashree, P. Vishnu Kamath, *J. Appl. Electrochem.* **2001**, 31, 1315–1320.

[86] P.V. Kamath, M. Dixit, L. Indira, A.K. Shukla, V.G. Kumar, N. Munichandraiah *J. Electrochem. Soc.* **1994**, 141, 2956–2959.

[87] Y.W. Li, J.H. Yao, C.J. Liu, W.M. Zhao, W.X. Deng, S.K. Zhong *Int. J. Hydrogen Energy* **2010**, 35, 2539–2545.

[88] J. Qi, P. Xu, Z. Lv, X. Liu, A. Wen *J. Alloys Compd.* **2008**, 462, 164–169.

[89] C.Y. Wang, S. Zhong, D.H. Bradhurst, H.K. Liu, S.X. Dou *J. Alloys Compd.* **2002**, 330–332, 802–805.

[90] Y.L. Zhao, J.M. Wang, H. Chen, T. Pan, J.Q. Zhang, C.N. Cao *Electrochim. Acta* **2004**, 50, 91–98.

[91] L. Demourgues-Guerlou, C. Delmas *J. Power Sources* **1993**, 45, 281–289.

[92] C. Liu, L. Huang, Y. Li, D. Sun *Ionics* **2010**, 16, 215–219.

[93] C. Delmas, J.J. Braconnier, Y. Borthomieu, P. Hagenmuller *Mater. Res. Bull.* **1987**, 22, 741–751.

[94] M. Dixit, P.V. Kamath, J. Gopalakrishnan *J. Electrochem. Soc.* **1999**, 146, 79–82.

[95] A. Wang, W.Zhou, Z. Sun, Z. Zhang, Z. Zhang, M. He, Q. Chen, *Molecular Catalysis*, **2021**, 499, 111276, 2468-8231.

[96] M.M.M. Pinto, M.E. Sousa, *Curr. Med. Chem.*, **2005**, 12, 2517-2538.

[97] C.N. Lin, H.K. Hsieh, S.J. Liou, H.H. Ko, H.C. Lin, M.I. Chung, F.N. Ko, H.W. Liu, C.M. Teng, *J. Pharm. Pharmacol.*, **1996**, 48, 887-890.

[98] W. Mahabusarakam, J. Proudfoot, W. Taylor, K. Croft, *Free Radic. Res.*, **2000**, 33, 643-659.

[99] P. Williams, M. Ongsakul, J. Proudfoot, K. Croft, L. Beilin, *Free Radic. Res.*, **1995**, 23, 175-184.

[100] Y.W. Cheng, J.J. Kang, *Eur. J. Pharmacol.*, **1997**, 336, 23-28.

[101] K. Nakatani, N. Nakahata, T. Arakawa, H. Yasuda, Y. Ohizumi, *Biochem. Pharmacol.*, **2002**, 63, 73-79.

[102] K. Nakatani, M. Atsumi, T. Arakawa, K. Oosawa, S. Shimura, N. Nakahata, Y. Ohizumi, *Biol. Pharm. Bull.*, **2002**, 25, 1137-1141.

[103] O. Suzuki, Y. Katsumata, M. Oya, V.M. Chari, B. Vermes, H. Wagner, K. Hostettman, *Planta Medica*, **1981,** 42(5), 17-21.

[104] S.S. Panda , M. Chand , R. Sakhuja, S.C. Jain, *Current Medicinal Chemistry*, **2013**, 20, 36, 4481-4507.

[105] J.A. Hernandez, S. A. Gomez, T. A. Zepeda, J. C. Fierro-Gonzalez, G. A. Fuentes, *ACS Catal*. **2015**, 5, 7, 4003–4012.

[106] S. Cao, Y. Zhao, S. Lee, S. Yang, J. Liu, G. Giannakakis, M. Li, M. Ouyang, D. Wang, E. C. H. Sykes, M. Flytzani-Stephanopoulos, , *Sci. Adv.* **2020**, 6, eaba3809.

[107] C.M Julien, M Massot, C Poinsignon, *Spectrochimica Acta Part A: Molecular and Biomolecular Spectroscopy*, **2004**, 60, 3, 689-700.

[108] V. Kisinger, I. Sander, P. Steiner, R. Zimmermman, S. Hufner, *Solid State Communications*, **1990**, 73, 7, 527-530.